NICER Monitoring of Supersoft X-Ray Sources

M. Orio[1,2] , K. Gendreau[3,4] , M. Giese[1], G. J. M. Luna[5,6,7] , J. Magdolen[8], S. Pei[9,10] , B. Sun[1,11], E. Behar[12] ,
A. Dobrotka[8], J. Mikolajewska[13] , Dheeraj R. Pasham[14], and T. E. Strohmayer[15]
[1] Department of Astronomy, University of Wisconsin 475 N. Charter Str., Madison, WI, USA; orio@astro.wisc.edu
[2] INAF-Padova, vicolo Osservatorio 5, I-35122 Padova, Italy; marina.orio@inaf.it
[3] Center for Exploration and Space Studies (CRESST), NASA/GSFC, Greenbelt, MD 20771, USA
[4] NASA Goddard Space Flight Center, Greenbelt, MD 20771, USA
[5] CONICET-Universidad de Buenos Aires, Instituto de Astronomía y Física del Espacio (IAFE), Av. Inte. Güiraldes 2620, C1428ZAA, Buenos Aires, Argentina
[6] Universidad de Buenos Aires, Facultad de Ciencias Exactas y Naturales, Buenos Aires, Argentina
[7] Universidad Nacional de Hurlingham, Av. Gdor. Vergara 2222, Villa Tesei, Buenos Aires, Argentina
[8] Advanced Technologies Research Institute, Faculty of Materials Science and Technology in Trnava, Slovak University of Technology in Bratislava, Bottova 25, 917
24 Trnava, Slovakia
[9] Department of Physics and Astronomy, Padova University, vicolo Osservatorio 3, I-35122 Padova, Italy
[10] School of Physics and Electrical Engineering, Liupanshui Normal University, Liupanshui, Guizhou, 553004, People's Republic of China
[11] Department of Physics and Astronomy, University of Missouri, Columbia, MO 65211, USA
[12] Department of Physics, Technion, Haifa, Israel
[13] Nicolaus Copernicus Astronomical Center of the Polish Academy of Sciences, Poland
[14] Kavli Institute for Astrophysics and Space Research, Massachusetts Institute of Technology, USA
[15] Astrophysics Science Division and Joint Space-Science Institute, NASA Goddard Space Flight Center, Greenbelt, MD 20771, USA

Abstract

We monitored four supersoft sources—two persistent ones, CAL 83 and MR Vel, and the recent novae YZ Ret (Nova Ret 2020), and V1674 Her (Nova Her 2021)—with NICER. The two persistent supersoft X-ray sources (SSS) were observed with unvaried X-ray flux level and spectrum, respectively, 13 and 20 yr after the last observations. Short-period modulations of the SSS appear where the spectrum of the luminous central source was fully visible (in CAL 83 and V1674 Her) and were absent in YZ Ret and MR Vel, in which the flux originated in photoionized or shocked plasma, while the white dwarf (WD) was not observable. We thus suggest that the pulsations occur on, or very close to, the WD surface. The pulsations of CAL 83 were almost unvaried after 15 yr, including an irregular drift of the $\simeq 67$ s period by 2.1 s. Simulations, including previous XMM-Newton data, indicate actual variations in period length within hours, rather than an artifact of the variable amplitude of the pulsations. Large amplitude pulsations with a period of 501.53 ± 0.30 s were always detected in V1674 Her, as long as the SSS was observable. This period seems to be due to rotation of a highly magnetized WD. We cannot confirm the maximum effective temperature of ($\simeq 145{,}000$ K) previously inferred for this nova, and discuss the difficulty in interpreting its spectrum. The WD appears to present two surface zones, one of which does not emit SSS flux.

Unified Astronomy Thesaurus concepts: Novae (1127)

1. Introduction

Supersoft X-ray sources (SSS) that are also sufficiently luminous at other wavelengths, allowing a clear classification, are found to be accreting white dwarfs (WDs), undergoing hydrogen burning in a shell close to the surface (see, among other articles, Orio 2013, and references therein). Often, they are transient SSS in post-outburst novae, in which hydrogen burning continues near the surface after the bulk of accreted envelope mass has been ejected and the WD photosphere has shrunk back to almost pre-outburst radius. The range of effective temperature $T_{\rm eff}$ in the SSS varies from $\simeq 120{,}000$ K to about a million K. Most post-AGB WDs that are still shell-burning hydrogen have larger envelopes than those of post-novae, and the average $T_{\rm eff}$ is much lower, often peaking only in the ultraviolet (see the objects studied by Córsico & Althaus 2014). There are a few exceptions, mainly PG 1159-type central stars of planetary nebulae, with $T_{\rm eff} > 100{,}000$ K

(Löbling et al. 2019; Adamczak et al. 2012). In the accreting WD of binaries, the burning shell is closer to the surface than in the post-AGB stars. In novae, convection brings to the surface $\beta+$ decaying nuclei that heat the envelope, so the average $T_{\rm eff}$ is the highest. Several post-outburst novae have been found to be close to the high end of the SSS temperature distribution (e.g., Ness et al. 2011; Orio et al. 2018). A nonnegligible group of non-novae, semi-steady or recurrent SSS, has been discovered in the Local Group (see Orio et al. 2010; Orio 2013), in directions of low-absorbing columns of gas. Especially in the Magellanic Clouds, many of these SSS have been identified with WD binaries in which accretion occurs onto the WD and hydrogen burning is ignited, but the process occurs at such a high rate that it does not cause thermonuclear runaways like in novae (see Yaron et al. 2005; Starrfield et al. 2012; Wolf et al. 2013, for the theoretical models). In this work, we observed again two of the non-nova close-binary SSS, extending the time line of their observations to over 20 yr for one of them (MR Vel) and $\simeq 40$ yr for the other one, CAL 83.

A very interesting characteristic of many SSS is the flux modulation with short periods, ranging from tens of seconds to $\simeq 1$ hr. In Table 1, we show a list of measured periods of

Table 1
Periods Measured in Supersoft X-Ray Sources

Object	Type	Period	References
RX J0648.0–4418	O subdwarf+WD	13.2 s	Mereghetti et al. (2009), Popov et al. (2018)
			Mereghetti et al. (2021)
N LMC 2009	nova	33.2 ± 0.1 s	Ness et al. (2015), Orio et al. (2021)
RS Oph	nova,symbiotic	34.9 ± 0.2 s	Nelson et al. (2008), Osborne et al. (2011), Pei et al. (2021b)
KT Eri	nova	34.83 ± 0.06 s	Ness et al. (2015), Pei et al. (2021c)
V339 Del	nova	54.1 ± 0.2 s	Ness et al. (2015)
CAL 83	main seq.+WD	$\simeq$67 s	Odendaal et al. (2014), Odendaal & Meintjes (2017)
V3890 Sgr	nova,symbiotic	$\simeq 82.9 \pm 0.6$ s	Beardmore et al. (2019), Page et al. (2020)
Chandra r2–12	semi-steady SSS	217.76 ± 0.05 s	Trudolyubov & Priedhorsky (2008), Chiosi et al. (2014)
Nova Her 2021	nova	501.35 ± 0.30 s	This work (see also Maccarone et al. 2021)
			Pei et al. (2021a), Drake et al. (2021)
V407 Lup	nova	565 s	Aydi et al. (2018), M. Orio (2022b, in preparation)
XMMU J004319.4+411759	nova?	865.5 ± 0.5 s	Osborne et al. (2001)
V4743 Sgr	nova	1325 s	Ness et al. (2003), Leibowitz et al. (2006)
			Zemko et al. (2016), Zemko et al. (2018)
V2491 Cyg	nova	2303.4 s	Ness et al. (2011), Ness et al. (2015), Zemko et al. (2015)
V1494 Aql	nova	2498.8 s	Drake et al. (2003), Rohrbach et al. (2009)
V959 Mon	nova	55 and 102 min.	Peretz et al. (2016)

semi-steady SSS and novae in the SSS phase, not including longer periods that have also been measured in some cases and have been found to be orbital in nature. The periods in the 5–45 minutes range measured in several novae, namely V407 Lup, V2491 Cyg, and V4743 Sgr, have been measured again at quiescence when the X-ray flux was $\simeq$5 orders of magnitude lower and the spectrum was less soft, as described in the references in Table 1. For these novae, the period has been attributed to the WD spin in a highly magnetized WD, an intermediate polar (IP) system. The period detection at quiescence is understood as due to the accretion curtain/pre-shock material absorbing the X-ray soft radiation of the hot polar caps differently as the WD rotates. It is not obvious why the SSS emission of the hydrogen burning WD is not homogeneous and why it shows a modulation with the rotation period. Probably, the WD is hotter at the poles, and/or the burning occurs closer to the surface and lasts longer at the poles, possibly fed by renewed accretion at the end of the outburst (see Zemko et al. 2016; Aydi et al. 2018, for a discussion). Understanding the mechanism of the modulations of the SSS post-outburst is essential to correctly model the outburst and the quiescent life of the systems.

Also in two non-nova SSS, the periodicity has been linked with the rotation period of the WD. In the WD with the shortest ever detected period of 13.2 s, RX J0648.0–4418, a negative period derivative has been measured, and has been interpreted as due to a young, contracting WD in a system containing a subdwarf as a close binary companion (Mereghetti et al. 2021, and references therein). In CAL83, a period of $\simeq$67 s has also been interpreted as linked with rotation. The period appeared to have a drift of about 3 s within short timescales, interpreted by Odendaal et al. (2014) as due to an envelope that is not quite synchronized with the rotation of the core WD, and by Odendaal & Meintjes (2017) as due to the effect of a weak ($\simeq 10^5$ G) magnetic field in an equatorial belt at the boundary with an accretion disk.

However, this model does not apply during the thermonuclear runaway, especially for the two pulsating recurrent novae (RN)/symbiotics, RS Oph and V3890 Sgr, which host a red giant and are thought to undergo disk accretion because of *atmospheric* Roche Lobe overflow (see Booth et al. 2016;

Mikołajewska et al. 2021). Ness et al. (2015) attributed the modulations to non-radial g-mode oscillations caused by the burning that induces gravity waves in the envelope (so called "ϵ mechanism"), but detailed calculations ruled out periods longer than $\simeq$10 s Wolf et al. (2018), leaving the puzzle unsolved.

With its excellent timing capabilities and high signal-to-noise ratio (S/N), especially in the soft X-ray range, the Neutron Star Interior Composition Explorer Mission (NICER) is an excellent instrument to study the SSS and their intriguing periodic modulations. The NICER camera is an external attached payload on the International Space Station (ISS). Although NICER's main task is to perform a fundamental investigation of the extreme physics of neutron stars, measuring their X-ray pulse profiles in order to better constrain the neutron star equation of state, NICER is useful for a variety of astrophysical targets. NICER provides also unprecedented timing-spectroscopy capability, with high throughput and low background (Prigozhin et al. 2016). The NICER instrument is the X-ray Timing Instrument (XTI), designed to detect the soft X-ray (0.2–12 keV) band emission from compact sources with both high time resolution and spectral information. It is a highly modular collection of X-ray concentrator (XRC) optics, each with an associated detector. The XTI collects cosmic X-rays using grazing-incidence, gold-coated aluminum foil optics, equipped with 56 pairs of XRC optic modules and a silicon-drift detector for high time-resolution observations (time-tagging resolution $\leqslant$300 ns). A shorter read-out time than other similar detectors on satellites in space (Chandra, XMM-Newton, Swift) allows significantly less pile-up, and this is ideal for supersoft X-ray sources.

This paper is structured as follows: each of the four sources we studied, CAL 83, MR Vel, V1674 Her, YZ Ret, is described in a separate section, with subsections describing the data and a brief discussion of the results. Finally, we summarize the results and draw some general conclusions in a final Conclusions section.

2. CAL 83: The "Oldest" Known SSS

CAL 83 was discovered by Einstein as one of the very first luminous SSS (Long et al. 1981). It is a close binary luminous

Table 2
Observations of CAL 83 with NICER, Exposure Time, Count Rate in the 0.2–1 keV Range, and "Softness Ratio" Measured as Ratio of Count Rate in the 0.2–0.35 keV Range versus Count Rate in the 0.35–1 keV Band

Observation ID	Start Time (UTC)	Exposure Time (s)	Mean Count Rate (cts s^{-1})	Softness Ratio (see text)
2611010101	2019-04-19,08:20:00	1104	6.000 ± 0.076	1.27
2611010102	2019-05-16,18:35:24	878	7.885 ± 0.097	1.06
2611010103	2019-05-17,21:09:30	996	8.197 ± 0.093	1.04
2611010104	2019-05-18,00:14:52	11057	7.405 ± 0.038	1.13
2611010105	2019-05-19,02:30:34	2763	6.866 ± 0.061	1.22
2611010106	2019-05-21,23:39:58	7632	8.343 ± 0.035	0.987

SSS in the Large Magellanic Cloud (LMC), never observed to undergo a nova outburst. The current understanding is that it hosts a massive WD accreting from a main sequence or slightly evolved companion, and it is luminous because of continuous shell nuclear burning. The luminosity due to the burning is orders of magnitudes higher than the accretion energy released in the disk. The accretion disk is instead a main contributor to the optical light, because it reprocesses X-rays from the disk in the optical energy range (Popham & di Stefano 1996). The nature of the companion is not well known. van den Heuvel et al. (1992) have argued that the donor star is more massive than the WD, while optical data analyzed by Crampton et al. (1987); Odendaal et al. (2014) seemed to show that the compact object is more massive than the donor.

CAL 83 has been observed to be extremely X-ray luminous for the last $\simeq 40$ yr. Occasional *off* states were observed for at least two days in 1999 November, during one day on 2001 October, and again twice in 2008 January and March, in observations spaced about 8 weeks apart (leaving us to wonder whether the off state lasted for the whole 8 weeks or longer). A week later in 2008, detection of intermediately high luminosity followed, but after two more weeks—in 2008 April—the source was again undetectable in two exposures, with a week interval in between. The sparse and irregular cadence of the observations (see Lanz et al. 2005; Odendaal et al. 2014) does not allow for drawing any clear conclusion on the duration of the "X-ray off" states. However, both Greiner & Di Stefano (2002) and Rajoelimanana et al. (2013) found that all "X-ray off" states were observed during optically bright states of the source, followed by a periodic dimming (by about 1 mag) about every 450 days. CAL 83 appeared X-ray luminous when the optical luminosity was lowest. Since the source of optical luminosity is the accretion disk, the reason for this apparent anticorrelation of X-ray and optical luminosity may be similar to the model proposed by Southwell et al. (1996) for RXJ0513-69, namely that photospheric contraction follows a period of high mass accretion rate $\dot{m}$ that triggers the burning, increasing the effective temperature of the WD and making the WD visible as a SSS. A periodic decrease in $\dot{m}$ may be followed by quenching of the burning and photospheric expansion after a certain time.

2.1. The NICER Observations of CAL83

The details of the observations are shown in Table 2. We obtained six observations on six different dates. An initial exposure of about 1 ks was done on 2019 April 19, to assess whether it had come out of a low state detected with Swift on 2019 April 15 in a 2 ks long exposure. It was found to be X-ray luminous again, after little less than 4 days. Five more

observations of a very different total duration were done between May 16 and May 21 of the same year, and no more *off* states were observed. While the work by Odendaal et al. (2014) focused on XMM-Newton continuous exposures with duration of hours, the NICER observations gave the opportunity to observe if and how the period changes over timescales of days and weeks. Frequent interruptions of the NICER exposures are due to the obstruction by the Earth, and the maximum exposure capacity for NICER is limited to ~ 1000 s. Moreover, during effective exposures, space weather conditions can also impact the quality of the data when there are flares in the background, due to the ISS being in certain regions near the poles or the South Atlantic Anomaly. Uninterrupted exposures of CAL 83 lasted from 208 to 1006 s, and exposures done on the same day, usually with intervals of order of $\simeq 5000$ s in between, were coadded in separate observations' data sets with the same observation number, and were archived as such in HEASARC.

2.2. Data Reduction of the NICER Exposures

HEASOFT version 6.29 c and NICER data-analysis software NICERDAS version 5.0 were used to reduce the data of the NICER observations. The timing analysis was performed with the Starlink PERIOD package, following the Lomb-Scargle (LS) method (Scargle 1982). Each light curve was first detrended, by subtracting a linear fit and dividing by the standard deviation. The PERIOD task SCARGLE was then used to create Lomb-Scargle periodograms (LSP) from each light curve. In the spectra of all the six NICER observations of CAL 83, all photons from the source are in the 0.2–1.0 keV energy region, so the light curves used to perform the timing analysis were extracted in this range. With the PERIOD task PEAKS, we found the highest peak in the periodogram between the frequencies that we specified, and in order to determine the statistical significance of the period and obtain a statistical error, we performed a Fisher randomization test, as described by Linnell Nemec & Nemec (1985), over frequencies from 10 to 100 mHz, including also red noise in the significance analysis. We did not subtract any background, which was very low compared to the source for most of the time, but we experimented with exclusions of intervals of high background by using two slightly different methods, with the `nicer_bkg_estimator` tool, which excludes periods of inclement "space weather," and the alternative `nibackgen3C50` tool, which uses a different method to choose the good time intervals (GTIs). Both tools are described in https://heasarc.gsfc.nasa.gov/docs/nicer/tools/nicer_bkg_est_tools.html. However, excluding high-background periods decreased the duration of the available observation, and the duration of
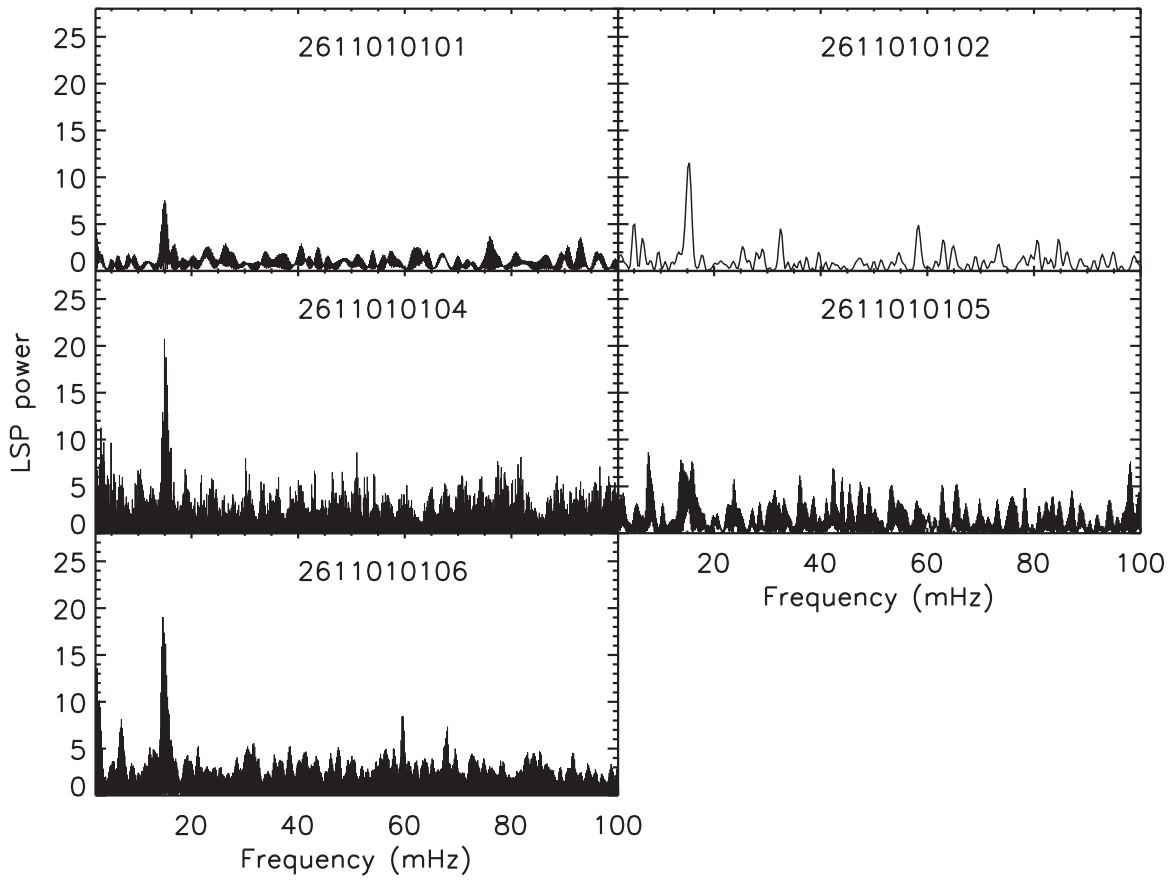
Figure 1. Periodograms of the observations of CAL 83 done on the different dates, with the peaks reported in column 2 of Table 2.

Table 3
Timing Analysis of NICER Light Curves of CAL 83 Showing the ∼67 s Pulsation

Observation ID	Period (s)	Significance (%)	Time (s)	Period (s)	Significance (%)	Time (s)	Period (s)	Significance (%)
	Whole light curve[a]			nicer_bkg_estimator[b]			nibackgen3C50[c]	
2611010101	66.6 ± 0.2	99.5	1100	66.7 ± 0.2	99.0	825	66.0 ± 0.2	98.5
2611010102	65.0 ± 1.2	99.0	877	65.0 ± 1.2	99.0	759	65.4 ± 1.3	99.5
2611010104	65.68 ± 0.01	99.0	8435	66.98 ± 0.02	99.0	9388	66.71 ± 0.02	99.0
2611010105	62.42 ± 0.08	44.5	2693	72.5 ± 0.1	32.8	2010	...	...
2611010106	66.85 ± 0.02	99.0	4040	68.25 ± 0.02	99.0	7305	65.67 ± 0.02	99.0

Notes.
[a] Using light curves in which the high-background periods are not excluded.
[b] Using light curves in which the high-background periods are excluded by using the nicer_bkg_estimator tool.
[c] Using light curves in which the high-background periods are excluded by using the nibackgen3C50 tool.

the light curve is important for the significance of the period searching by using the LS method.

2.3. Results of the NICER Observations

Table 3 shows the results obtained with the LS period search with three differently filtered data sets: using all the available exposure time and not excluding the high background periods, excluding high background periods by using the `nicer_bk-g_estimator` tool, and finally also using the `nibackgen3C50` tool. Periodograms obtained for different dates shown in Figure 1, and the light curves folded with the periods listed in the second column of Table 3 are shown in Figure 2.

Because the actual time intervals considered in each exposure without exclusion of adverse space weather and with the two different methods are slightly different, we measured slightly different periods. This difference, we found, is actually due to the fact that the period is always found to drift within timescales of minutes and hours, so even excluding different, short time intervals (that is, using different GTIs) yields different results. With the last correction method, the period was not detected in observation 261100105 of 2019 May 19, and there is only a low significance detection in the first two columns. We suggest that the reason for which the period becomes undetectable during short continuous exposure is in
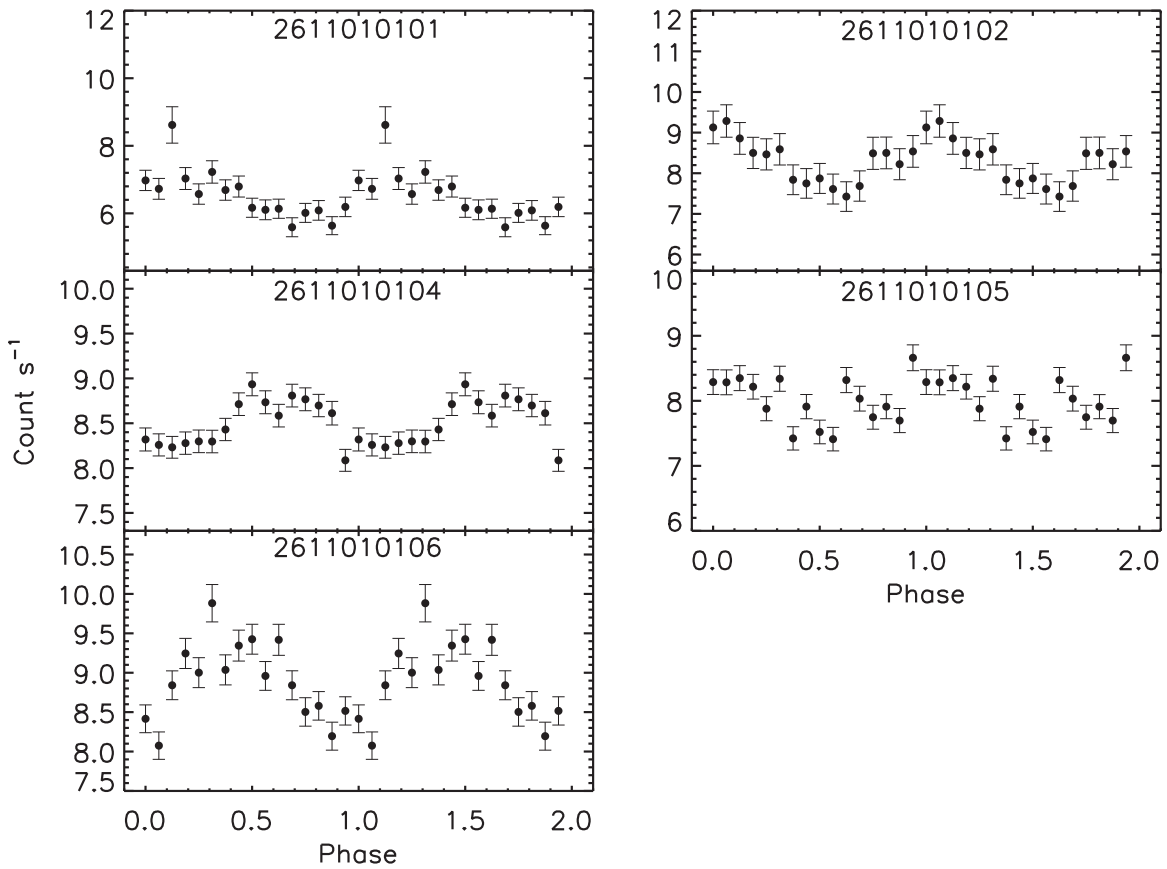
Figure 2. Light curves of CAL 83 in the 0.2–1.0 keV range, corrected with the nicer_bkg_estimator tool, folded with the periods found in Table 2.

the variable amplitude of the modulation, which becomes too small for detections at times. We do not find evidence that the periodicity is transient. We also note that, with both methods of excluding bad space weather, the results are consistent within statistical errors with the whole light curve in 3 out of 4 observations with a high probability detection.

However, the detected periods are not consistent with each other on the different dates, showing a clear variation from one day to the other. The variation is not dependent on the average count rate during the exposure, indicating that we cannot correlate the average count rate with the length of the measured period. The periodograms obtained with the data set in column 2 of Table 3 are shown in Figures 1, and 2, showing the light curves folded with the measured periods. Table 4 shows that we did not find significant differences in the modulation amplitude of the ~67 s period in the light curves extracted in both the 0.2–0.4 keV range and in the 0.4–1 keV range. Thus, the modulation is not energy-dependent in the 0.2–1 keV in which CAL 83 is X-ray luminous.

Table 5 shows the results of the analysis of the single short exposures, excluding the intervals of poor space weather only with the nicer_bkg_estimator tool. Here we evaluated the statistical error for the frequency by fitting a Gaussian to the highest peak in the periodogram, when this fit was possible. We retrieved the frequency with high significance only in 7 of the single short intervals of uninterrupted exposures, and the statistical error in the frequency is quite large. Realizing that the errors are very large, we did not perform a statistical test to evaluate the errors better like we did for the "total" observations in Table 3. We stress that, again, we did not find

Table 4
Modulation Amplitudes of the ~67 s Pulsation in the 0.2–0.4 keV and 0.4–1.0 keV Light Curves of CAL 83, Defined as (max–min)/(max+min).

Observation ID	Period[a] (s)	Modulation Amplitude (%) 0.2–0.4 keV	Modulation Amplitude (%) 0.4–1.0 keV
2611010101	66.70	22.4	27.2
2611010102	65.00	16.2	17.1
2611010104	66.98	4.0	8.2
2611010105	72.50	8.1	11.0
2611010106	68.25	7.6	8.7

Notes. The high-background periods are excluded by using the nicer_bkg_estimator tool.
[a] The period used to fold the corresponding light curves of CAL 83 in Figure 2.

a correlation between average count rate during the exposure and frequency measured in the exposure. We attribute the difficulty to measure the period during the short continuous observations to the varying amplitude of the pulsation. Since it appears to vary when we fold the single light curves with the period that was detected, we suggest in some exposures it must have been too low for a clear measurement, and that it is unlikely that the period was transient.

2.4. Simulating the CAL 83 Data for Better Understanding

Simulations of the periodic variability of nova V4743 Sgr done by Dobrotka & Ness (2017) showed that a double-peak pattern found in the periodogram was not caused by two actual different

Table 5
Detailed Analysis Using LSP on the Light Curves of the Single Uninterrupted Short Exposures of CAL 83 Done with NICER, Corrected for Bad Space Weather with the nicer_bkg_estimator Tool

Obs. ID	Seg.	Start Time (UT)	Exp. (s)	Freq. (mHz)	P(s)	Sig. (%)
2611010101	1	2019 April 19 08:24:36	405	14.37 ± 0.85	69.6	<10
	2	2019 April 19 09:57:13	708	14.99 ± 0.46	66.7	94.7
2611010102	1	2019 May 16 18:35:24	872	15.22 ± 0.62	65.7	86.4
2611010103	1	2019 May 17 21:11:52	205	⋯	⋯	⋯
	2	2019 May 17 22:44:36	670	15.22 ± 0.85	65.7	<10
2611010104	1	2019 May 18 00:17:19	769	⋯	⋯	⋯
	2	2019 May 18 01:50:01	791	⋯	⋯	⋯
	3	2019 May 18 03:24:15	714	15.26 ± 0.65	65.5	<10
	4	2019 May 18 04:35:06	408	⋯	⋯	⋯
	5	2019 May 18 04:58:41	628	15.03 ± 0.80	66.5	98.7
	6	2019 May 18 06:07:49	379	⋯	⋯	⋯
	7	2019 May 18 06:33:09	545	14.44	69.3	<10
	9	2019 May 18 08:06:37	519	14.30	69.9	<10
	11	2019 May 18 09:39:18	538	15.11	66.2	<10
	12	2019 May 18 12:41:11	779	⋯	⋯	⋯
	14	2019 May 18 14:18:26	507	15.19 ± 0.66	65.8	<10
	15	2019 May 18 15:24:05	830(553)	⋯	⋯	⋯
	16	2019 May 18 15:54:54	280	15.54 ± 1.61	64.4	<10
	17	2019 May 18 20:02:14	907	15.02 ± 0.63	66.6	99.9
2611010105	1	2019 May 19 02:33:11	921	⋯	⋯	⋯
	2	2019 May 19 04:05:54	920	15.17 ± 0.53	65.9	50.3
	3	2019 May 19 05:39:44	854	⋯	⋯	⋯
2611010106	1	2019 May 21 23:47:04	1006(373)	14.86	67.3	<10
	2	2019 May 22 01:25:08	699	⋯	⋯	⋯
	3	2019 May 22 04:26:48	143	⋯	⋯	⋯
	6	2019 May 22 12:21:10	279	14.78 ± 1.86	67.4	98.9
	8	2019 May 22 15:16:58	644	14.91 ± 0.85	67.0	68.2
	9	2019 May 22 16:49:09	854	15.03 ± 0.65	66.5	99.9
	10	2019 May 22 18:22:33	960	⋯	⋯	⋯

Note. We include observation ID (Obs. ID), observation number, observation segment, which is a continuous exposure (Seg.), starting date and time, effective exposure duration in seconds (Exp.), LSP frequency with highest significance (Freq.), 1σ error of the LSP frequency (Err.), corresponding period (P), and significance (Sig.). Segments 8, 10, 13 in observation 2611010104 and segments 4, 5, 7 in 2611010106 were not analyzed because of bad space-weather conditions. In the exposure column, the number in parenthesis is the total exposure time after the exposure was corrected for bad space weather. No error is given for the frequency when a Gaussian fit was not possible.

frequencies, but originated in a single frequency with amplitude variability, causing a false beating. In Orio et al. (2021), we could not rule out that the measured period drift for N LMC 2009 was an artifact of variable amplitude, even if detailed simulations showed that an actual variation of the period was more likely. In order to assess whether the period drift measured in CAL 83 is real, or an artifact due to the variable amplitude of the oscillation, we resorted to simulations.

The period was modeled as a sinusoidal function

$$\psi = \phi + a \sin(2\pi t/p) \tag{1}$$

where ϕ is the mean period value[16] in the observed data. Poisson noise was then added. The simulations were performed

---

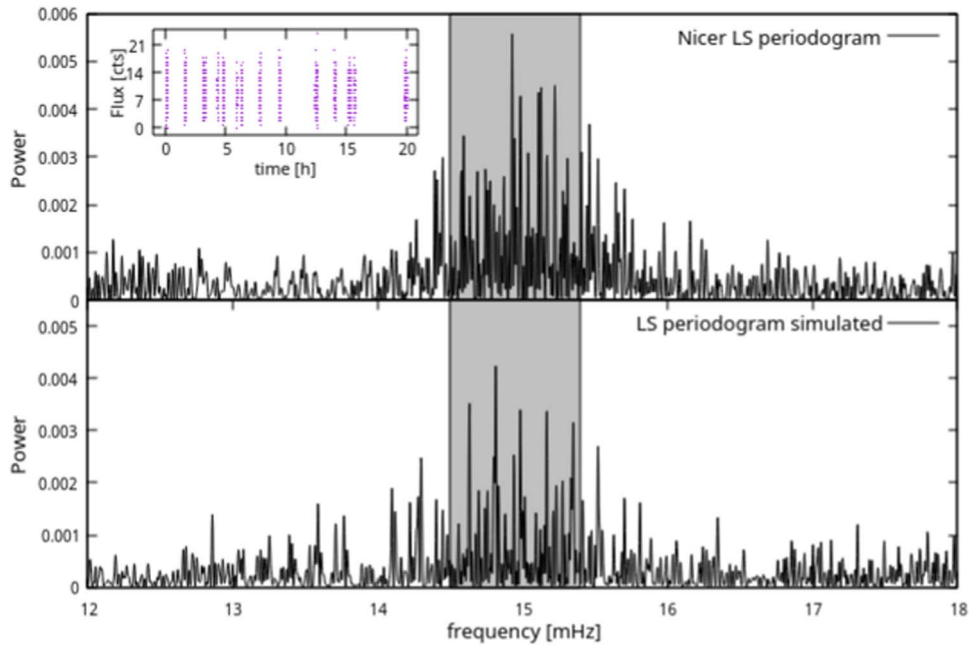[16] No long-term trend was noticeable.

Figure 3. The LS periodogram of the observed NICER data of CAL 83 (top panel), and a simulated LS periodogram (lower panel), modulated with constant amplitude and constant period. The inset shows the corresponding light curve that consists of 15 partial observations. The gray shaded area represents the interval from which the p values were randomly selected for the simulation.

by varying either only one of the two a and p parameters or both of them at the same time, to examine how the actual variations affect the amplitude and/or the period that we measure.

In order to simulate the variability, we selected randomly generated points in Gaussian curves centered on the mean value of a or p, and selected variance values corresponding to typical values in the actual periodograms. We chose the input for the sine function by randomly selecting the values of a polynomial (P_a and P_p) of an order between 10 and 30. If the amplitude was negative, we assumed $a = 0$. The sinusoidal function thus can be written as follows:

$$\psi = \phi + P_a \sin(2\pi t/P_p). \qquad (2)$$

For the three types of variability (var_a, $var_a + var_p$, var_p) we run 1,000,000 simulations, creating LSPs. We selected the periodogram that best simulates the data, by calculating the sum of the residual squares $\sum(o - s)^2$ calculated over a given period interval, where o is the observed power and s the simulated one.

We performed these simulations for the light curve of NICER observation 2611010104 shown in Table 5, consisting of 15 partial exposures (Figure 3 inset; note that we neglected the intervals without any measured value, and split one interval of Table 3 in two parts, because there was a small gap during the exposure). Besides the detected ∼67 s period, some randomly selected p mean values between 65 s and 69 s (gray shaded area in Figure 3) were also used. We chose the best 100 results for each type of variability by examining the sum of the residual squares, and compared the observed and simulated LS periodograms. 52 of the best periodograms were simulated with variable amplitude and constant period, 23 with constant amplitude and variable period, and 25 with variable amplitude and period.

The result indicates that the constant and variable period fit the data equally well. However, Figure 3 (bottom panel) shows

the simulated LS periodogram in which the light curve was modulated with constant amplitude and constant period. It is clear that it is affected by significant aliasing because of the different duration of the partial observations and intervals between them. Thus, complicated patterns of variability cannot be analyzed.

In order to eliminate the aliasing problem, we repeated the simulation with the same p values, splitting the light curve in the short continuous exposures listed in Table 3, and created an LS periodogram for each short exposure. The duration of the individual continuous exposures varies from 240 to 907 s, and as shown in Table 3, was often not sufficiently long for clear detections of the periodicity. In the simulations, we found the following distribution for the 100 periodograms with the best residuals: 48 with variable amplitude and constant frequency, 17 with constant amplitude and variable frequency, 35 with variable amplitude and variable frequency. However, the LS periodograms have very broad peaks, which in most cases we could not reproduce, so this simulation did not lead to a clear conclusion. Figure 2 of Odendaal et al. (2014), based on XMM-Newton data, shows that the width of the frequency drift due to potentially variable periodicity is approximately 1–2 mHz (see observation ID or ObsID 0506531701). Considering $1/T$ (where T is the duration of a continuous exposure) as periodogram resolution, even the longest NICER snapshot of 907 s yields a resolution of 1.1 mHz, which is comparable to the width of the frequency drift and does not allow a detailed analysis. As a test, we repeated the simulations only with exposures longer than 500 s (a limit that was empirically based on visual inspection of the periodograms) and found a different result, namely 94 of the 100 best simulations had variable amplitude and fixed frequency. Thus, the results of these simulations of the many short NICER exposures depend on the minimum length chosen to select the exposures to model.
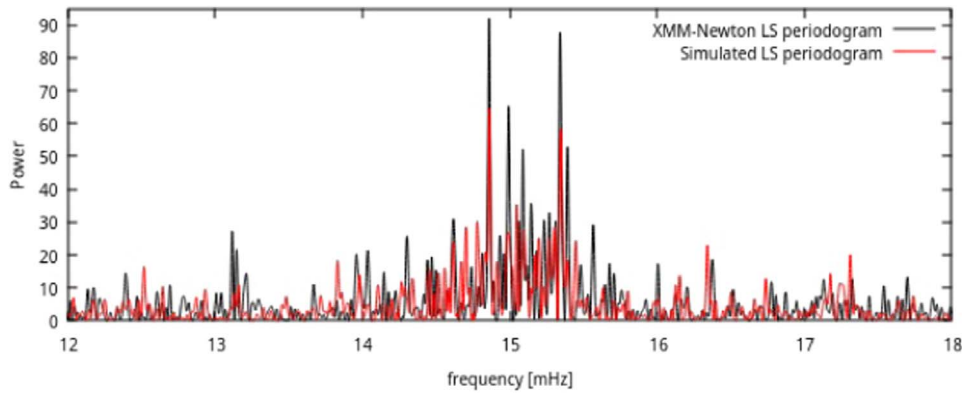
Figure 4. The best-simulated LS periodogram for the XMM-Newton observation of CAL83 started on 2009 May 30 and lasting 46 ks. The light curve was modulated with constant amplitude and variable period.

We conclude that the analysis should be based on much longer continuous exposures and repeated the simulation for the XMM-Newton EPIC-pn light curve of ObsID 0506531701, the most recent and longest continuous exposure among all X-ray observations of CAL 83 (see Odendaal et al. 2014). As Figure 3, bottom right panel, shows, this continuous exposure gave a complex result, with other minor peaks in the periodograms that were relatively high. We adopted the following mean values: $p = 65.2$ s , $p = 66.3$ s, $p = 66.7$ s, $p = 67.3$ s, corresponding to the highest peaks around the observed ∼67 s periodicity, and a value between them. We modeled the long-term trend of the observed light curve by assuming that the vertical shift ϕ resulted from a polynomial fit (13th order, P_{13}). Again, we selected the 100 fits with the best residuals, obtaining the following outcome: 87 were with constant amplitude and variable period, 13 with variable amplitude and variable period, none with a constant period. The best-simulated LS periodogram is shown in Figure 4.

With the result obtained with the XMM-Newton data, we draw the conclusions that CAL 83 has a variable period, ruling out that the observed LS periodogram is modulated by a stable period with variable amplitude (even if also the amplitude varies). As mentioned above, Orio et al. (2021) were able to model the periodogram of Nova LMC 2009a in the SSS phase even only with variable amplitude, but a variable period appeared to yield better simulations. While in the LMC 2009a, the scattering was around 0.4 s; in CAL 83 it is quite longer, namely 2.1 s, allowing for a more definite conclusion.

2.5. CAL 83 Spectra Observed with NICER

CAL 83 was observed with the Chandra Low Energy Transmission Grating (LETG) in 2001 May and with XMM-Newton once in 2001 and in several exposures between 2007 and 2008. Two LETG exposures in 2002 October found the source in an *off* state. Because of the shorter NICER read-out time, the spectra are not affected by pile-up in this extremely soft source, like EPIC and the Chandra ACIS-S (an observation was done with this instrument in 1999), but CAL 83 is too soft for the XMM-Newton Reflection Grating Spectrometers (RGS) grating, which does not measure the whole spectral range of interest. Therefore, we compare the NICER spectra with the ones observed in 2001 with the LETG, despite the very different spectral resolution. The average count rate of CAL 83 has always varied in different observations (see Odendaal et al. 2014), and an interesting question is whether there is a correlation with spectral variations. In

Figure 5, in the top panel on the right, we compare the NICER average spectra on different days, and we also show the comparison with the LETG spectrum of 2001. One of the 2019 NICER spectra, and the LETG 2001 one, are shown fitted with atmospheric models in the lower panels of Figure 5, in units of energy and wavelength, respectively. A rigorous fit was done by Lanz et al. (2005), who found a best fit with with $\log(g) = 8.5$ and $T_{\rm eff} = 550{,}000 \pm 2500$ K, fixed $N({\rm H}) = 6.5 \times 10^{20}$ cm^{-2}, absolute luminosity $1.8 \pm 0.6 \times 10^{37}$ erg s^{-1}. These author's atmospheric models are not public, so we used the publicly available TMAP code grid of models of Rauch et al. (2010), available in the website http://astro.uni-tuebingen.de/#rauch/TMAP/TMAP.html. We find the best fit to the NICER spectrum of May 18 (the longest exposure) with a model studied for Magellanic Cloud and Galactic halo sources with depleted abundances, with $\log(g) = 9.0$. Model "halo" with $\log(g) = 9$, which we used, is adopted from a grid of models with only elements from H to Ca, which is defined as "not suitable for precise spectral analysis" because only approximate formulae were used in order to account for Stark line broadening. However, with the broadband spectra, the absorption lines are not measurable and great precision is not required. The more rigorously calculated grid with elements up to Ni has peculiar abundances adopted from specific nova models (see Rauch et al. 2010), so we found that the depleted-abundances model is more suitable, as expected because the Magellanic Clouds have low metallicity, and no strong mixing like in post-novae should have occurred in CAL 83. All the public grids in the website are either with $\log(g) = 8$ or $\log(g) = 9$, but no available models were computed with values between these two extremes. $\log(g) = 9$ models fit better than those with $\log(g) = 8$, but the fit we obtain is not perfect, mainly because it underpredicts the flux above 0.5 keV. The values we obtain are close to those of Lanz et al. (2005), but the higher $\log(g)$ results in a lower temperature, namely $T_{\rm eff} = 502{,}000 \pm 5000$ K, $N({\rm H}) = 5.1 \times 10^{20}$ cm^{-2}, absorbed flux 7.4×10^{-12} erg s^{-1} cm^{-2} and unabsorbed flux 3.5×10^{-11} erg s^{-1} cm^{-2}. We find that this model fits also the LETG spectrum of 2001, with $T_{\rm eff} = 469{,}000 \pm 5000$ K, $N({\rm H}) = 6.3 \times 10^{20}$ cm^{-2}, absorbed flux 8.3×10^{-12} erg s^{-1} cm^{-2}, unabsorbed flux 5.6×10^{-11} erg s^{-1} cm^{-2} (corresponding to an absolute luminosity of 1.67×10^{37} erg s^{-1} at a distance of 50 kpc to the LMC). However, if we model the LETG spectrum with more bins, we obtain a better result with the grid studied for nova abundances (specifically, model SSS-003-00010-00060.bin-0.002-9), because it includes more ions and thus models the absorption features. The resulting parameters are $T_{\rm eff} = 505{,}000 \pm 5000$ K, $N({\rm H}) = 5.8 \times 10^{20}$ cm^{-2}, absorbed flux 7.9×10^{-12} erg s^{-1} cm^{-2}, unabsorbed
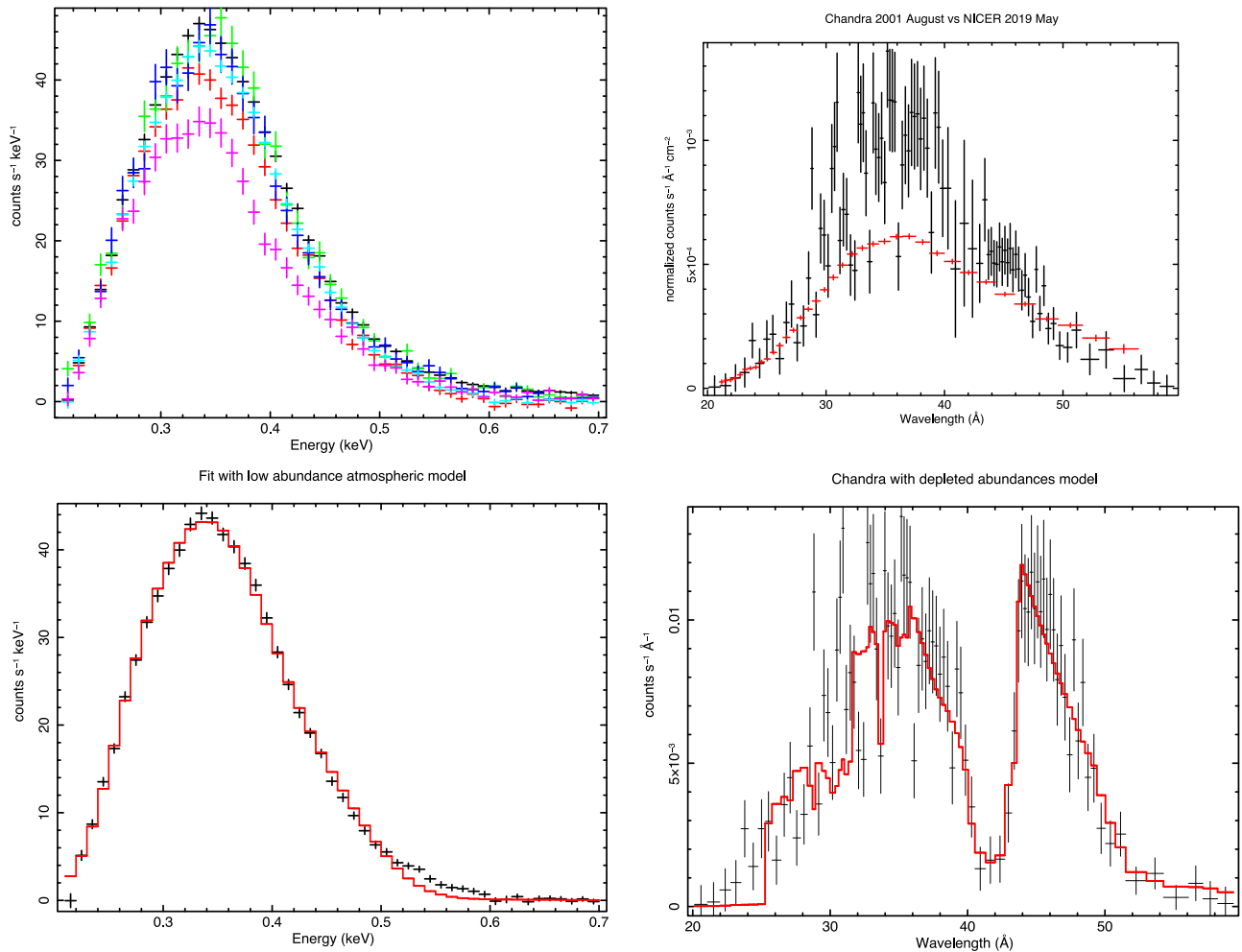
Figure 5. The top panel on the left shows the CAL83 average-count-rate spectra measured during each day of NICER observations, done in 2019. The top panel on the right, in units of wavelength appropriate for the grating spectrum, shows the comparison between the fluxed spectrum (normalized for the effective area) measured on May 21 with NICER (the one with the largest count rate) with the fluxed 2001 Chandra LETG spectrum (again as a function of wavelength to respect the gratings scale), binned with large bins of S/N—at least S/N = 100 per bin—for a better comparison with NICER. There was excess flux in 2001, but the peak and spectral shape seem unchanged. In the bottom panels, we show fits to the 2001 Chandra (right) and 2019 NICER (left) count-rate spectra, respectively, with the abundance-depleted atmospheric model discussed and referenced in the text and the same parameters.

flux 4.5×10^{-11} erg s^{-1} cm^{-2} (corresponding to absolute luminosity 1.34×10^{37} erg s^{-1}). Since we did not have a sufficiently *sensitive* grid of log(g) values, the small differences in the best-fits' parameters (of order 10%) are within each other's statistical errors and do not indicate any significant spectral difference between 2001 and 2019.

Because the peak of the count rate is around 0.35 keV, in Table 2, we also give the "softness ratio" measured as count rate in the 0.2–0.35 keV band divided by count rate in the 0.35–1 keV band. It is evident from the table that this ratio decreases when the total count rate increases; thus when the average count rate is lower, the softest portion increases. We also tried to estimate the flux in two energy ranges, the softest, namely 0.2–0.3 keV and the total flux in the 0.2–0.8 keV range (there is hardly any flux above 0.8 keV). We did so by fitting the model described above, choosing on purpose the softest possible range for this comparison. We found that the unabsorbed flux in this softest band varies by at most 15% around an average $\simeq 2.1 \times 10^{-12}$ erg cm^{-2} s^{-1}. The total range in the whole 0.2–0.8 keV range of interest also varies by about 15% around an average value of $\simeq 7 \times 10^{-12}$ erg cm^{-2} s^{-1}. From these two indications, "softness ratio" and comparison of

flux estimates, we infer that the measured-count-rate variation is not due to change in column density N(H), as would be the case if it was due, for instance, to a wind.

2.6. Accretion and Burning in CAL 83

Odendaal & Meintjes (2017) offered an attractive explanation for the oscillations in the X-ray flux of CAL 83, as a "dwarf nova oscillation" type of quasi periodic oscillation in a "belt-like structure" at the boundary of the inner accretion disk, which is weakly coupled with the WD core by a $\simeq 10^5$ G magnetic field, rotating faster than the WD itself and with a combination of spin-up and spin-down. However, the high S/N obtained with NICER in the softest range (0.2–0.4 keV) demonstrates that the modulation is not energy-dependent. The accretion belt is very unlikely to emit such conspicuous flux in the very soft energy band of 0.2–0.4 keV. Since we attribute the extremely high flux in this range only to the WD atmospheric emission, the pulsation appears to be occurring on the WD.

Odendaal & Meintjes (2017) did not quantify all aspects of the model for the case of CAL 83, and spectral predictions are missing in the paper, but since accretion would produce a much

less luminous and much less soft emission than observed, the absence of energy dependence may be a strong point against the so-called eLIMA model of these authors. The short-period oscillations with a period drift observed in RS Oph and V3890 Sgr, which are symbiotic systems, during their nova eruption, are also unlikely to be explained by such a model. The accretion disks in symbiotics have very different sizes and characteristics, and there is evidence that at least the inner accretion disk is destroyed during the eruption (Worters et al. 2007). In the 2006 outburst, the accretion disk of RS Oph was only reestablished by day 241 of the outburst, long after the SSS turn-off (Worters et al. 2007). A common model for all the shortest-period modulations of the SSS seems desirable, even if only for an *Occam's razor* criterion.

Another important point raised by the NICER monitoring is that the SSS flux always appears to vary by up to 30%, even within hours, without spectral hardening that may indicate increased absorption. Moreover, we observed that the rise from the minimum X-ray luminosity $L_X \leqslant 10^{36}$ erg s^{-1} to an X-ray luminosity level above 10^{37} erg s^{-1} took only 3 days, and the source was never observed again at minimum in the course of 5 days in 2019 May. A successful explanation of the luminosity variations of CAL 83, attributed either to photospheric adjustments or to variable accretion (see Greiner & Di Stefano 2002), has to take these timescales into account.

3. MR Vel: An "Extreme" Symbiotic Star

MR Vel (RX J0927.5–4758) is a peculiar steady X-ray source, initially observed with ROSAT and later observed and found equally luminous with ASCA, BeppoSAX, Chandra, and XMM-Newton, with a highly absorbed ($N(\mathrm{H}) \simeq 10^{22}$ cm^{-2}), yet found with supersoft X-ray spectrum due mainly to emission lines (see Bearda et al. 2002; Motch et al. 2002, and references therein). Despite the relatively low inclination, estimated to be between $50° \leqslant i \leqslant 60°$ (according to Schmidtke et al. 2000), the X-ray grating spectra show an emission-line spectrum that cannot be fitted with models of collisional ionization or photoionization and is difficult to explain. The absorbed X-ray luminosity is about 10^{35} erg s^{-1} at a distance of 1 kpc, but GAIA indicates a value of $5.68^{+1.00}_{-0.74}$ kpc (Bailer-Jones et al. 2021).

The orbital period of MR Vel is 4.028 days (Schmidtke et al. 2000; Schmidtke & Cowley 2001), and the optical light curve also shows modulations with periods of 0.2 to 0.3 days—a 0.2 days modulation was also observed in X-rays in the year 2000 (see Motch et al. 2002; Bearda et al. 2002, and references therein). The radial velocities of the He II 4686 and Hα emission lines and their amplitude allowed us to estimate a mass range of 1–2 $M_\odot$ for the donor, and of 0.7–1.7 $M_\odot$ for the accreting object (Schmidtke et al. 2000; Schmidtke & Cowley 2001). So far, no trace of the donor has been detected in the optical spectrum (Schmidtke et al. 2000), nor in the *I* band (Mennickent et al. 2003). In June 1997, Motch (1998) detected transient jets from MR Vel with projected velocity of 5200 km s^{-1}. The receding component of the Hα jet with projected velocity of 5350 km s^{-1} was tentatively identified by Schmidtke et al. (2000) in 1999 March. For the majority of jets, the outflow velocity reflects the escape velocity at their origin (Livio 1998), and assuming that the jet expansion is perpendicular to the orbital plane, the expansion velocity is $\sim 8100 \leqslant V_{\exp} = V_{\mathrm{jet}} \cos i^{-1} \leqslant 13{,}000$ km s^{-1} for the inclination range given above ($50° \leqslant i \leqslant 60°$). This is consistent with
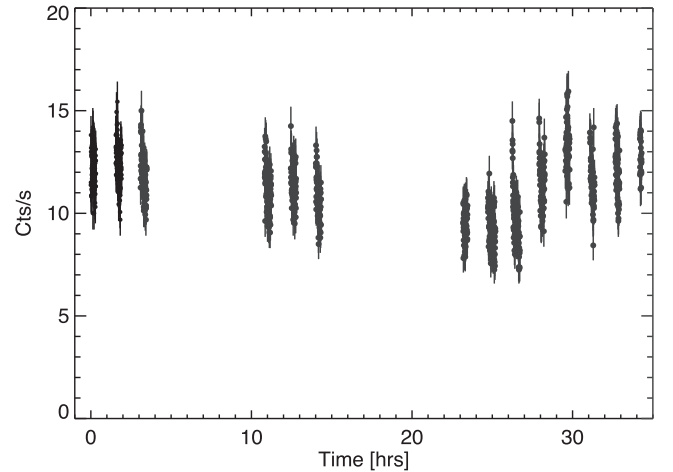

Figure 6. The light curve of MR Vel observed with NICER from 2019 May 19 until 2019 May 20 with time bins of 16 s.

a massive, ~ 1–1.3 $M_\odot$, WD accretor, and narrows the range for the mass of the donor, $M_1 \sim 1$–1.6 $M_\odot$. For a binary period of about 4 days and the above mass range, the Roche-lobe radius of a main-sequence secondary should be of the order of $R_2 \sim 1$–1.5 $R_\odot$; thus a donor star with mass ~ 1–1.6 $M_\odot$ fitting this system must be evolved. The effective temperature of this donor does not exceed ~ 6000 K, and the luminosity does not exceed ~ 30 $L_\odot$. The Two Micron All Sky Survey magnitudes of MR Vel, $J = 12.934 \pm 0.029$, H $= 12.204 \pm 0.102$, $K = 11.770 \pm 0.024$ provide some additional constraints. The source is highly reddened, as indicated by the neutral-hydrogen column density, $N_H \simeq 10^{22}$ cm^{-2}, which corresponds to a reddening of $E(B - V) \simeq 1.4$–1.6 (adopting the conversion relationship given by Güver & Özel 2009). The reddening corrected $(J - K)_0 \sim 0.4$–0.5 is thus consistent with a G2–8 giant ($T_{\mathrm{eff}} \sim 5000$–5600 K); moreover the magnitude $K_0 \sim 11.2 - 11.3$ combined with the Gaia distance indicates a luminosity of ~ 110–180 $L_\odot$. The radius of such a star, ~ 14 $R_\odot$, would be almost $3\times$ larger than the Roche-lobe radius. Summarizing, the observational data are consistent with a low-mass, 1–1.6 $M_\odot$, yellow (G-type) giant donor ascending the first giant branch, and a massive, 1–1.3 $M_\odot$, WD secondary. So, in principle, MR Vel is likely to be a sort of extreme (with the shortest orbital period!) yellow symbiotic system, similar to, e.g., StHA 190 (Smith et al. 2001).

3.1. The NICER Observations of MR Vel

We observed MR Vel with NICER in several exposures lasting about 1000 s each on 2019 May 18 and 19. The data reduction was performed as described above for CAL 83, and the data we present had bad space-weather intervals subtracted with the nibackgen3C50 tool. Figure 6 shows the light curve observed in the 0.2–12 keV range of NICER. We could not conclude anything definite about the orbital modulation, although the variability observed over 35 hr, namely the apparent modulation in Figure 6, supports this possibility. Figure 7 also shows that, even if there are spectral variations within hours, there have not been major differences on timescales of hours (NICER-NICER comparison, panel on the left) or of years (panel on the right, with the Chandra HETG and XMM-Newton RGS grating spectra compared to the spectrum observed with NICER). There were some small, but exceeding the cross-calibration uncertainties, flux differences
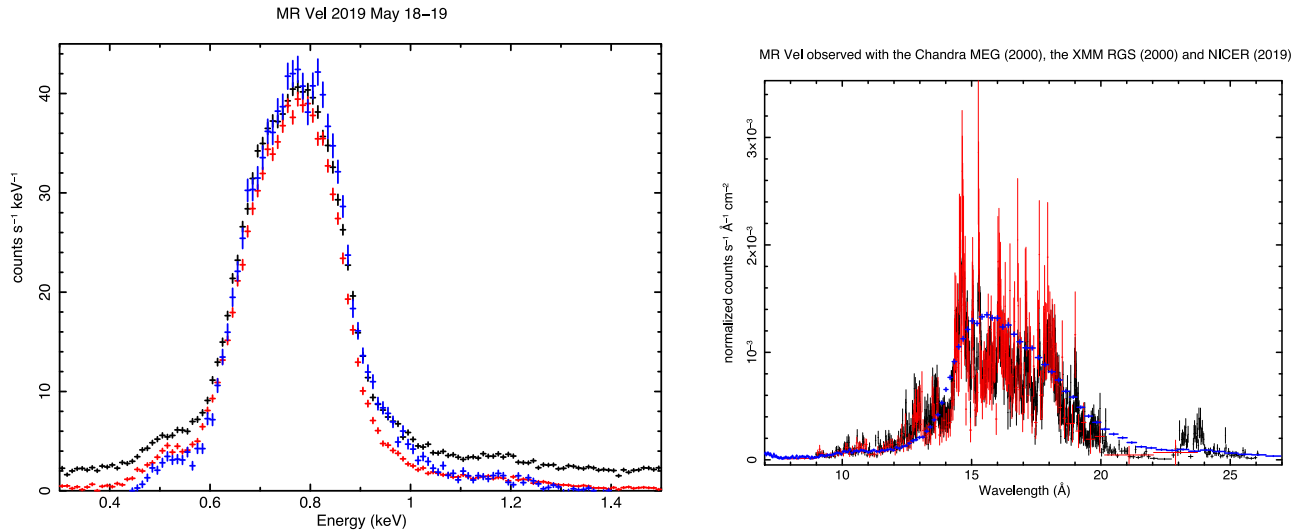
Figure 7. On the left, the energy/count-rate spectra of MR Vel observed with NICER in three different observations composed of coadded individual exposures (see Figure 6), and on the right, comparison of the grating spectra, fluxed (normalized for effective area) and plotted in their natural wavelength units, observed in 2000 with the Chandra MEG grating (red), and with the XMM-Newton RGS gratings (black) with the 2021 May 18 spectra observed with NICER (blue, plotted here also as a function of wavelength for comparison.)

between NICER exposures, and between the average spectrum observed in 2000 and in 2021. These variations were both in the soft and the hard tail of the spectrum, so they do not seem to be due to variable, intrinsic absorption.

4. V1674 Her (Nova Her 2021): A Magnetic Nova

This nova was discovered as the transient TCP J18573095 +1653396 on 2021 June 12.537 UT at mag. 8.4 by Seiji Ueda (Kushiro, Hokkaido, Japan). Munari et al. (2021) reported optical spectroscopic confirmation that this was indeed a nova in outburst. The optical decay from optical maximum—around $V = 6.2$—is quantified as t_2 (time for a decay by 2 mag) and was as short as $\simeq$2.5 days. Few novae have such a rapid decrease from peak optical luminosity, indicating a very energetic phenomenon. Like YZ Ret, V1674 Her in outburst was detected at all wavelengths from IR to gamma-rays (Aydi et al. 2020; Li 2021). The nova was observed in 2021 June with Swift, and the X-Ray Telescope (XRT) did not detect a source between 2021 June 13 and 2021 June 18. After almost a week after the optical maximum, on 2021 June 18, a hard X-ray source appeared, followed on 2021 July 1 by the initial rise of a luminous, supersoft X-ray source.

A modulation with a periodicity of 501.4277 ± 0.0002 s was discovered in archival Zwicky Transient Facility images by Mroz et al. (2021), Drake et al. (2021), and it was followed by the discovery that a very close period is measurable in the supersoft X-ray source that appeared shortly after the outburst. Maccarone et al. (2021) reported a modulation with a 503.9 s period in a Chandra observation done for 10 ks on 2021 July 10 with the HRC-S camera, and in Pei et al. (2021a), we reported a modulation with a 501.8 ± 0.7 s period in the initial NICER data. A second Chandra observation by Drake et al. (2021) revealed a period of 501.72 ± 0.11 s in the 0-order light curve of an exposure of 30 ks done with the Chandra HRC-S camera and LETG. The period measured at optical wavelengths before the outburst is not consistent, within the error estimate, with the one measured with Chandra by Drake et al. (2021), or even with a new, recent optical period of 501.516 ± 0.018 s measured by Patterson et al. (2021). Assuming the period is

the one of the WD rotation, this is an indication of spin-down due to ejected mass in the range $0.2–2 \times 10^{-4}$ $M_\odot$. In a paper by (A. Dobrotka et al. 2022, in preparation), a group of us will reexamine the Chandra light curves and try to determine whether, given the superimposed aperiodic variability and the nonsinusoidal shape of the modulation, the conclusion of a period change and/or different optical and X-ray periods can be confirmed. However, here we examine only the NICER data.

The fact that the period detected at optical wavelength at quiescence is very close to the one detected in supersoft X-rays in outburst has been interpreted as an indication that Nova Her may host a magnetized WD, in an IP system. These systems host WDs whose magnetic field strengths reach several 10^5 Gauss. An accretion disk forms, but it is truncated where the ram pressure of the matter in the disk is equal to the magnetic pressure of the WD's magnetic field (at the Alfvèn radius), and the matter is channeled to the poles. WDs in IPs are not synchronized with the orbital period like the more magnetized polars, and since the magnetic axes of the WD are generally inclined with respect to their rotation axes, the asynchronous primary is an oblique rotator. X-ray flux modulation with the WD-spin period is one of the main observational properties, considered the best indirect proof of the IP nature in many systems in which direct measurements of circular polarization with current instrumentation yield only upper limits for the magnetic field. The cause of the short (around a minute) period modulation of the supersoft X-rays in an outburst is not fully understood, but the modulation has been attributed to the WD rotation in three other recent novae in outbursts, with periods of several minutes, detected again at quiescence, along with typical signatures of IPs: V4743 Sgr (Ness et al. 2003; Leibowitz et al. 2006; Dobrotka & Ness 2017), V2491 Cyg (Ness et al. 2011; Zemko et al. 2015, 2018), and V407 Lup (Aydi et al. 2018, and paper by M. Orio et al. 2022a, in preparation). As described above for one of the proposed explanations for CAL 83, the modulation of the supersoft X-rays indicates nonhomogeneous temperature on the surface of the WD, which presumably is hotter at the poles.
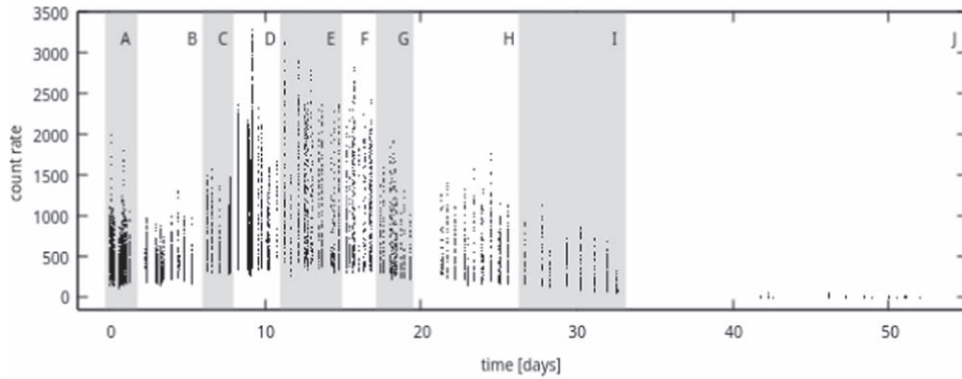
Figure 8. The light curve of V1674 Her observed with NICER since 2021 July 10 at UT 18:28:40, binned with 16 s bins. The very large modulation amplitude with the $\simeq$501 s period in each single observation, and superimposed random variability, is evident from the spread of the points.
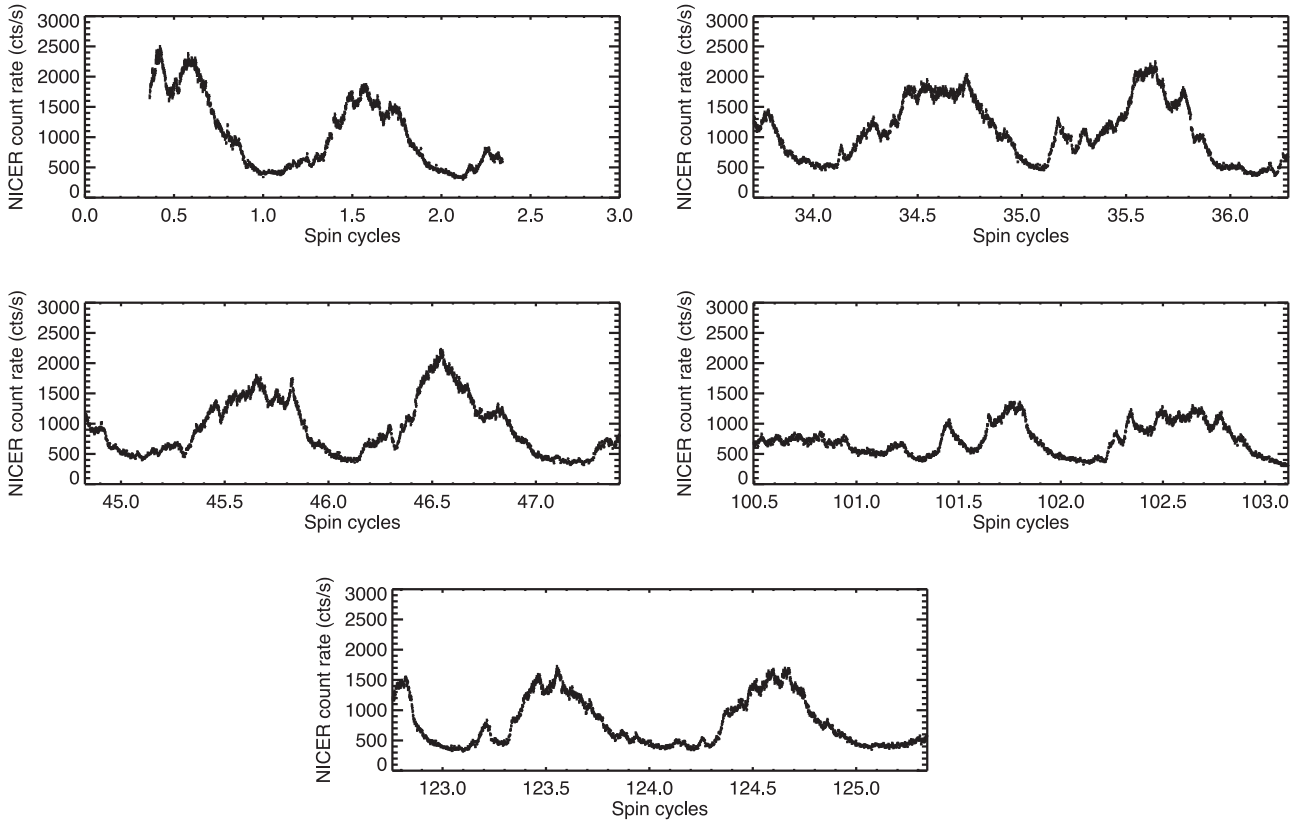

Figure 9. Light curves of the GTIs of July 20 observations of V1674 Her (4202260108), during interval D of Figure 8, binned with 1 s bins and plotted as a function of the elapsed phases, assuming a zero-point in the first minimum observed on that day.

4.1. The NICER Observations of V1674 Her and Their Timing Analysis

V1674 Her was monitored with NICER on 45 different dates between 2021/07/10 and 2021/08/31, with daily frequency whenever it was possible. The X-ray light curve was previously followed with the Swift-XRT, and although there always was a detectable X-ray source from the third day after optical maximum, initially there was a faint, nonsupersoft X-ray source, most likely due to shocks in the ejected matter (see Drake et al. 2021).

We started the NICER monitoring only after the luminous, supersoft X-ray source was observed to rise with Swift. The data were again reduced as described for CAL 83, and the light curve that we measured is shown in Figure 8. The NICER exposures were not always continuous, and the total exposure

time in one day varied from 476 s (not sufficiently long for period detection) to 15,782 s. The modulation with the $\simeq$501 s period is very clear throughout the whole period of NICER observations, including the late exposures when the count rate had decreased significantly (interval J in Figure 8). However, there was also irregular variability almost every day, on timescales of a few seconds, and Figures 9 and 10 show two examples of variability observed only within 24 hr in each case.

In Figure 11, we show periodograms of the NICER exposures done in the time intervals marked from A to J in Figure 8, namely from 2021 July 11 until 2021 July 12, from 2021 July 13 until 2021 July 22, from July 22 to August 1, from August 1 to August 8, and from that day until August 31. The peak frequency, listed in Table 6, is always clearly detected, until the end of the NICER observations, and always
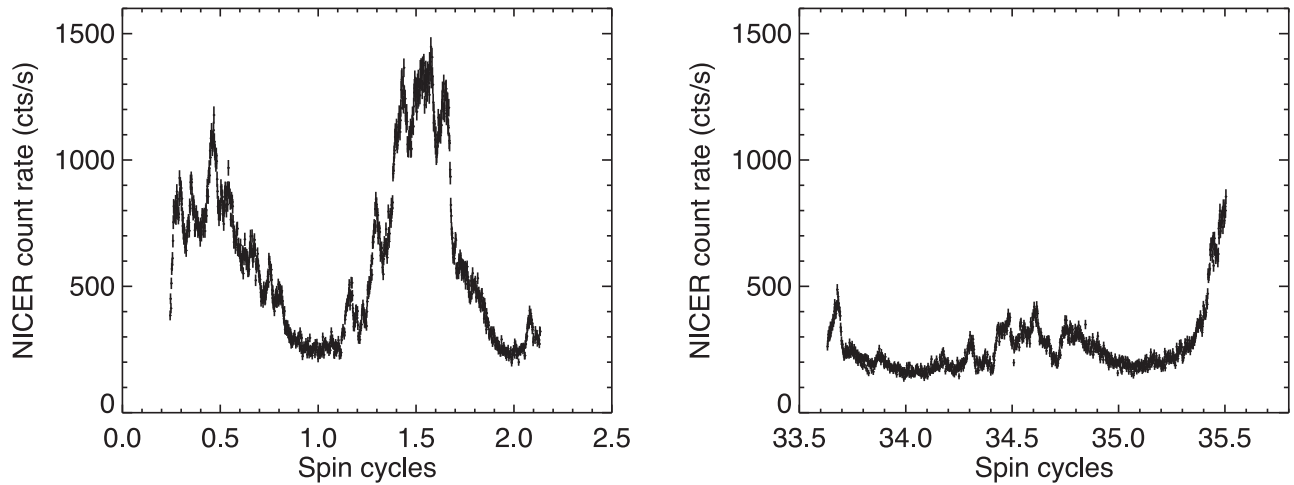
Figure 10. Light curves of the GTIs of August 2 observations of V1674 Her (4202260120), during interval G of Figure 8, binned with 1 s bins and plotted as a function of phase, again assuming a zero-point in the first minimum of that day.

falls within the error derived in each interval. Because of the spacing between the single short exposures, in some cases covering even only one whole period, the plots show several aliases, but it is clear that the main frequency peak, corresponding to an average period 501.535 s, is well detected and unique. The peak frequency is always the same within a small uncertainty that we estimated by fitting a Gaussian to the peak of the power spectrum, and is also listed in Table 6. The derived uncertainty in the period was only -0.300 s when the S/N is the highest, and became $-1.330/+1.340$ s when the source was fading. Although the Gaussian fitting method gives a rather conservative estimate of the error compared with statistical methods, given the superimposed aperiodic variability, we preferred it, and in this case, we did not perform a Fisher randomization test. We concluded that the NICER data do not support the strong conclusions on the spin-down derived in Drake et al. (2021). As the light curve in Figure 8 shows, the total unabsorbed average flux decreased since the beginning of August, and the source was observed with NICER until August 31, when the count rate had decreased to 1.385 ± 0.059 cts s^{-1}. New observations with the Swift-XRT were done on September 9, 26–27, and October 10–15, still detecting the SSS with about constant flux between August 30 and October 16, and with a very similar X-ray spectral shape (see Figure 15). The period was detected until the end of the NICER monitoring. We do not know whether the present X-ray flux is representative of the quiescent level over the next few years, because there may still be accelerated accretion due to irradiation, but since the quiescent IPs X-ray luminosity is on average larger than 10^{32} erg s^{-1}, at a distance of $\simeq 5$ kpc (see discussion Drake et al. 2021, and references therein), we expect that V1674 Her will still be detectable in a few months after the nova has returned to quiescence, and detecting the period in the accreting quiescent source will be an important test of its IP nature.

4.2. The X-Ray Spectral Evolution of Nova Her 2021

Drake et al. (2021) do not discuss spectral models that fits the Chandra LETG spectrum observed on 2021 July 19 by their collaboration, limiting the analysis to identifying spectral lines. However, they also present Swift-XRT monitoring and examine simple models to fit the Swift X-ray spectra of the

nova. They find a fit with a blackbody with four added absorption edges (assumed to be of N VI at 0.55 keV, N VII at 0.67 keV, O VII at 0.74 keV, and O VIII at 0.87 keV to simulate typical edges observed in such a hot atmosphere), or with the model grid we used above for CAL 83 and solar abundances, specifically the rauch-H-Ca-solar-90.fits model. They suggest a constant column density $N(\mathrm{H}) = 2.9 \times 10^{-21}$ cm^{-2} (approximately the value estimated in the direction of the nova, without intrinsic contribution) and a constant blackbody temperature of about 61 eV between days 18.9 and 27.7 after the optical maximum. After this period, the blackbody temperature increased and reached an astounding value of 125 eV (145,000 K) on day 44.2, later oscillating between 65 and 85 eV. Although we confirm the goodness of these fits to many of the Swift data, the better S/N, larger calibrated energy range, and same or better spectral resolution of NICER (Prigozhin et al. 2016) allow us to observe a more structured spectrum than the one measured with Swift, and reveal that the models used for Swift are not adequate for better quality spectra.

For the average NICER spectra of different exposures, both on the same day and on different dates, we measured a very similar spectral shape. However, in Figure 12, we show the spectra extracted during the first exposure done on 2021 July 20 in short ($\simeq$100–150 s) intervals around the maxima and minima, normalized to the level of count rate in the 0.2–0.4 cts s^{-1} range of the first of the two maxima. We notice some hardening during minima, which appears evident when we compare the *softness ratio*, which for this source we defined as the ratio of the count rate in the 0.2–0.5 keV divided by the count rate in the 0.5–1.0 keV: 0.25 and 0.27 for the two maxima, and 2.77 and 2.41 during the minima. This difference indicates that the flux decrease may be due to column density variations. We repeated the exercise for maxima and minima during other GTIs and exposures, finding that, around the time of the minima, we consistently seem to measure a larger ratio of the count rate in the 0.5–10 keV range to that in the 0.2–0.5 keV range than around the maxima. The "high state" average spectrum versus "low state" average spectrum comparison in Figure 3 of Drake et al. (2021) for the Chandra spectrum around minima showed more flux compared to the continuum level for emission lines of iron in the 0.776–0.886 keV region, of O VIII at 0.654 keV and O VII at 0.574 keV, and of N VII at 0.500 keV, than the average
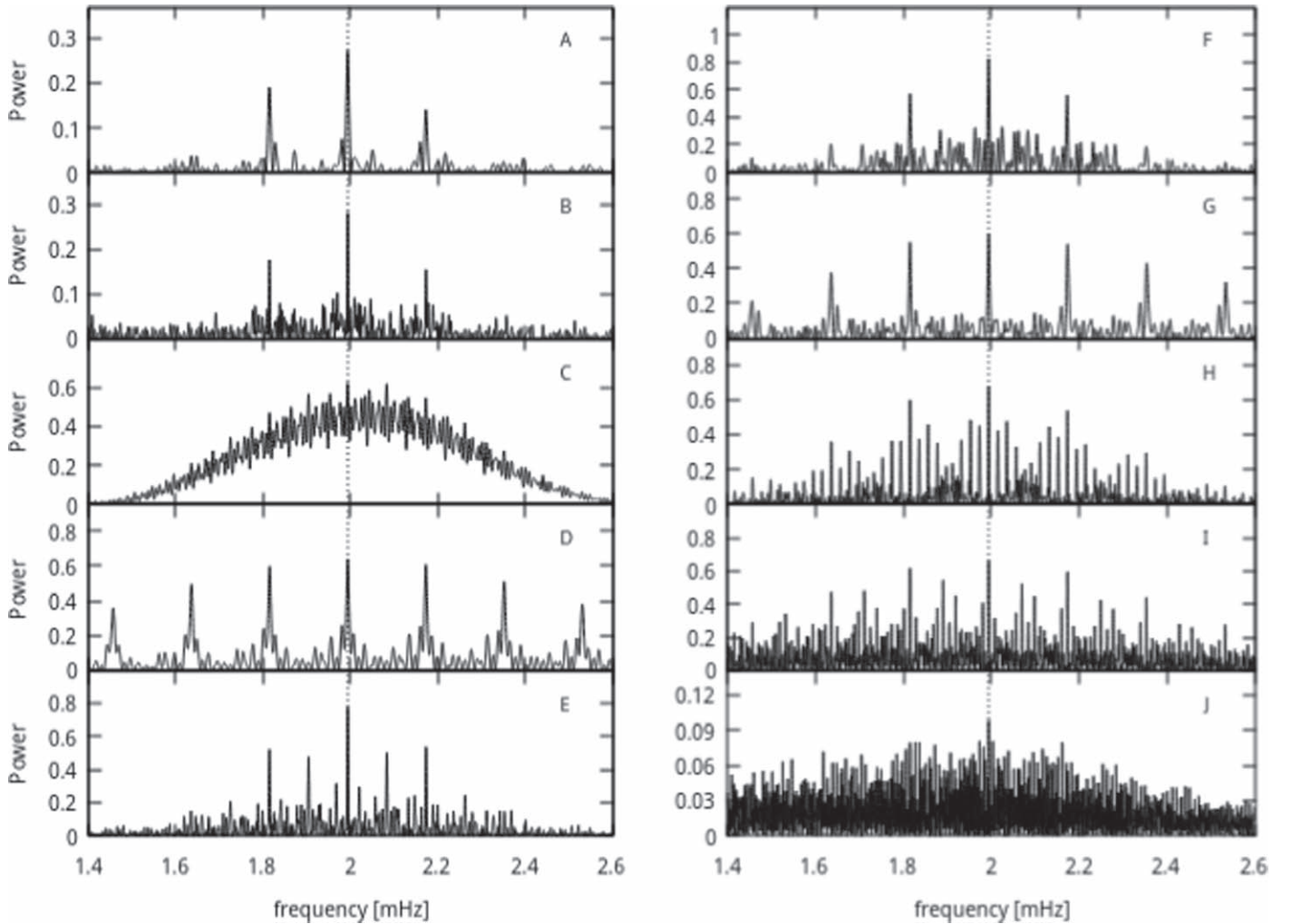
Figure 11. The top panel shows the periodograms of the summed exposures of V1674 Her done since the beginning of the observations in the periods marked in Figure 8.

Table 6
Frequency Peak in the Different Time Intervals Shown in Figure 8 in the Light Curve of V1674 Her

Time Interval	Frequency Peak (mHz)
A	1.9938 ± 0.0031
B	1.9939 ± 0.0012
C	1.9935 ± 0.0044
D	1.9939 ± 0.0033
E	1.9939 ± 0.0012
F	1.9937 ± 0.0021
G	1.9940 ± 0.0024
H	1.9939 ± 0.0009
I	1.9939 ± 0.0006
J	1.9939 ± 0.0004

spectrum extracted close to the maxima. These emission lines are not resolved with NICER, so even comparing maximum and minimum spectra obtained during the same period cycle does not allow to clarify whether the less soft spectrum is due to emission lines that are more prominent above the continuum. We cannot rule out that the variation is due only to the plasma that emits the emission lines, rather than to the WD atmospheric flux, which at this temperature should have only absorption features (Rauch et al. 2010).

We also suggest that the difficulty in fitting the data, at least since July 13, is due to these strong emission lines, measurable only in the single Chandra grating exposure. In Figure 13, we show the NICER spectrum observed on 2021 July 19 and the Chandra LETG spectrum observed on the same day, which is complex and rich in both emission and absorption features. We also overplot the fit to both spectra with a blackbody and absorption edges used for the Swift spectra of the same period (Drake et al. 2021). Figure 14 shows the best fit that we obtained for the NICER data with only one component, but it is not rigorous, yielding a reduced χ^2 value larger than 1. The deviation from an atmospheric spectrum through the emission lines appears clearly in the panel on the right, showing the Chandra spectrum. The prominent, superimposed emission lines, must originate in one or more additional components. We concluded that the blackbody with absorption edges is not a significant model for the SSS phase of V1674 Her, and that the effective temperature of the WD cannot be estimated in this way.

Until we have a rigorous model for the Chandra LETG spectrum of the supersoft source (which should be the subject of an upcoming paper), we cannot draw any conclusions on the effective temperature, which is related to the WD mass. We note that the atmospheric fits are closer to converging only
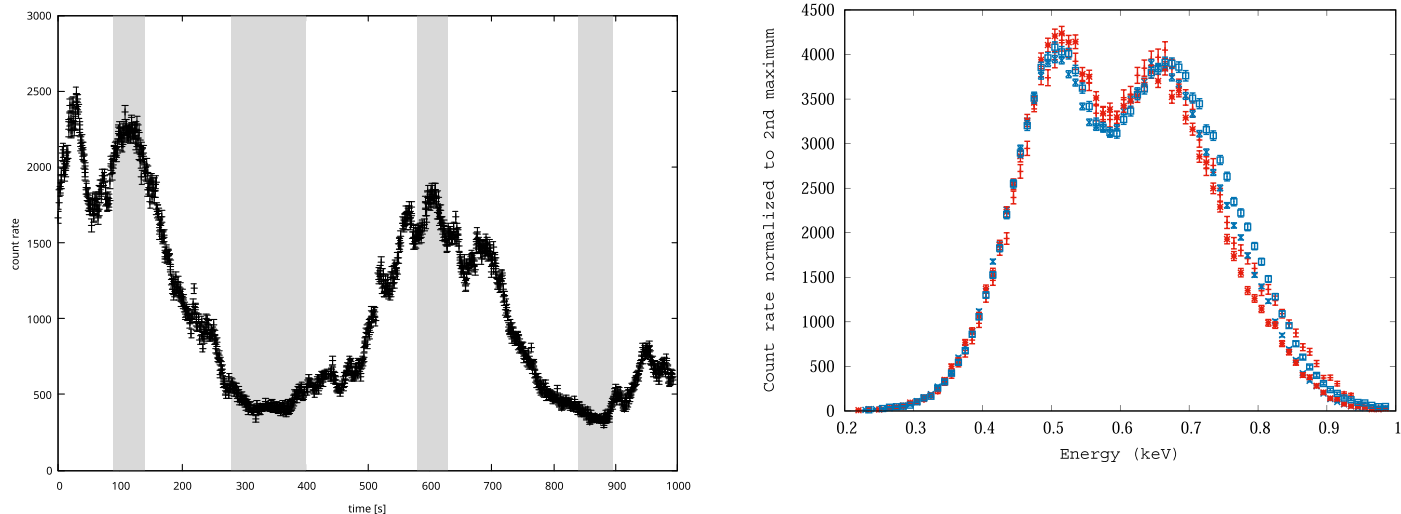
Figure 12. The spectra extracted around maxima and minima (shaded areas) of the first exposure done on July 20 are shown on the right. The spectra traced in blue are extracted from the minima shaded on the light curve shown on the left, the red from the minima. The count rate has been normalized to the level of the second maximum, by multiplying the first maximum spectrum (red stars) by 0.7, and the minima respectively by 3.2 (first minimum, x-es), and by 2.7 (second minimum, squares).
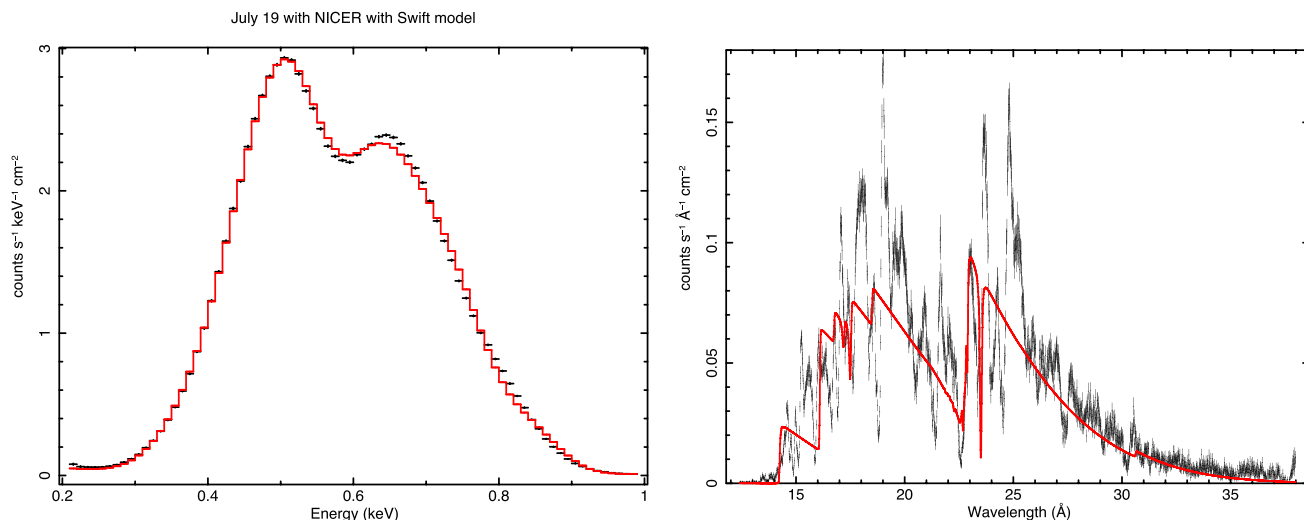

Figure 13. The spectrum of V1674 Her on the left, plotted as a function of energy, was measured on July 19. The LETG spectrum plotted on the right with the natural units of wavelength of the grating was also measured on the same day, although at a different time. The best fit with the blackbody+edges model of Drake et al. (2021) is shown in both panels. The fit is not perfect for the NICER spectrum, and since in the LETG, we are able to resolve the absorption and emission lines; it is clear that this one-component fit is not adequate.

using the grid without enhanced abundances, and at a temperature not exceeding 900,000 K, which is significantly lower than the temperature obtained with the fits to the Swift spectra (Drake et al. 2021) with blackbody and absorption edges (the column density in this case N(H) would be higher). However, the only definite conclusion that we can draw is not based on the model fits, and is that by comparison with other novae's SSS spectra (see Figure 3 of Drake et al. 2021) V1674 Her was quite "harder" than average, indicating a very massive WD.

One interesting characteristic of two novae that in recent years have been found to be IPs is that the supersoft luminosity emission region appeared to shrink rather than cool during the luminosity decay (Page 2012; Aydi et al. 2018). In Figure 15, we show that this seems to have been the case also for V1674 Her. If the SSS was cooling, it was only by a very small amount, as the source flux was decreasing much faster than

what may be attributed to decreasing temperature. A likely interpretation is that the burning ended later at the poles than in the rest of the WD, possibly fed by renewed accretion. Also in quiescence, three IP-novae retained a very soft emission region, albeit at much lower luminosity, with about the same effective temperature as the nova in the outburst (Zemko et al. 2015, 2016), and paper by M. Orio et al. (2022a, in preparation).

5. YZ Ret: A So-far-unique "VY Scl" Nova

YZ Ret (Nova Ret 2020, also called EC03572-5455 and MGAB-V207 in different surveys) was discovered in outburst on 2020 July 11.76 at magnitude $V \simeq 5$ by Mc Naught (2020, CBET, 4811, 1), but the nova was unreported for about a week, because pre-discovery images were later examined, and the nova was found to have erupted on 2020 July 08.171 (see Sokolovsky et al. 2021, and references therein). It was
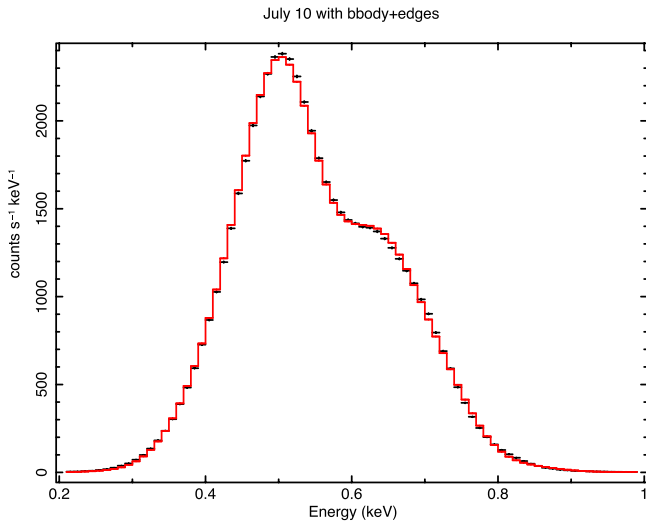
Figure 14. The initial NICER spectrum of of V1674 Her during the bright phase, on July 10, (observations 4622010101), is shown here. It is fitted with a blackbody with absorption edges like in Drake et al. (2021), but from July 13, the deviations from a one-component fit seem to grow and even increase with time.
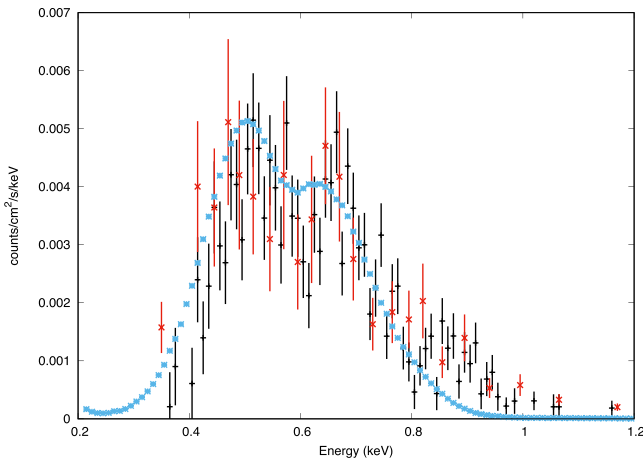

Figure 15. Spectra of V1674 Her observed during the decay phase: the one observed with NICER on 2021 August 3 (observation 4202260121) is plotted again in light blue divided by a normalization factor of 330. The spectrum observed with NICER on 2021 August 30 (observation 4202260139) is plotted in black, and the one observed with the Swift-XRT on 2021 October 15–16 is plotted in red.

classified as a nova in eruption thanks to the optical spectra first obtained by Aydi et al. (2020). Two peculiarities made this nova interesting for our study: in the first place, it is the first known VY Scl system to have been observed in a nova outburst (see Li et al. 2020; Sokolovsky et al. 2021). VY Scl are nova-like binaries that undergo transient periods of fading of the optical light by 1.5 to 7 mag in less than 150 days, lasting from weeks to years. In the more common *high state*, VY Scl have large optical and UV luminosity, and this is interpreted as evidence that most of the time mass transfer onto the WD occurs at the high rate $\dot{m} > 10^{-10}\ M_{\odot}\ \mathrm{yr}^{-1}$, to sustain an accretion disk in a stable hot state in which dwarf novae outbursts are suppressed. The low states have been attributed to a sudden drop of $\dot{m}$ from the secondary, or even to a total cessation of mass transfer (King & Cannizzo 1998; Hessman 2000); perhaps due to spots on the surface of the secondary
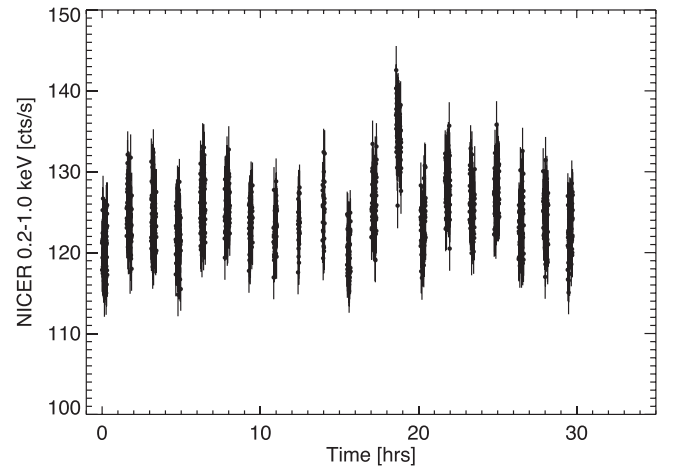

Figure 16. Light curve of YZ Ret observed with NICER with 16 s time bins, on 2021 September 28 and 29.

covering the L1 point (Livio & Pringle 1994) or none-quilibrium of the irradiated atmosphere of the donor (see Wu et al. 1995).

Monitoring the X-rays emission of a few VY Scl WD binaries, no indications have been found of a previously hypothesized SSS, expected with high $\dot{m}$ because of non-explosive thermonuclear burning (see Zemko et al. 2014, and references therein). At least for one VY Scl, V794 Aql, there is no clear correlation between optical and X-ray luminosity (Sun et al. 2020). Mass transfer may be very irregular or sporadic for these systems, due to a complicated interplay between the two binary components affecting the thermal state of the donor. YZ Ret has proven that even if thermonuclear burning does occur, it must last for quite some time and end in a nova outburst, instead of being steady and without outflows as expected for SNe Ia progenitors (e.g., models by van den Heuvel et al. 1992).

The other peculiarity of this nova is that, unlike most Galactic novae that are often concentrated toward the Galactic bulge, it is located away from the Galactic plane, with a very low column density of only about $1.2–1.3 \times 10^{20}\ \mathrm{cm}^{-2}$.

5.1. NICER Observations of YZ Ret

We observed the nova with NICER in 20 intervals of about 1000 s each, during an overall time of 29.71 hr starting on 2020 September 28 at 15:25:44 UT. The light curve over all this period of observation is shown in Figure 16. No periodic modulation could be detected in the NICER light curve.

In Pei et al. (2020), we announced the observation and measurement of the X-ray source. We found that, since the column density was known and the distance determined with the GAIA parallax is $2.7^{+0.4}_{-0.3}$ kpc (Bailer-Jones et al. 2018), an attempt to fit the spectrum with an atmospheric model yielded a relatively poor fit, but was sufficient to obtain an order of magnitude of the X-ray flux. We found that the X-ray luminosity was too low to be originating from all, of most of, the surface of a hydrogen-burning WD, only about 2.5×10^{35} erg s^{-1} (see Figure 17). We confirm this result: the closest fit obtained with a model atmosphere (nova model SSS_003_00010-00060.bin_0.002_9.00.fits in the grid by Rauch, see above) yields a reduced χ^2 of 1.37 with 75° of freedom, with $T_{\mathrm{eff}} = 534{,}000$ K and $N(\mathrm{H}) = 3.3 \times 10^{20}\ \mathrm{cm}^{-2}$.
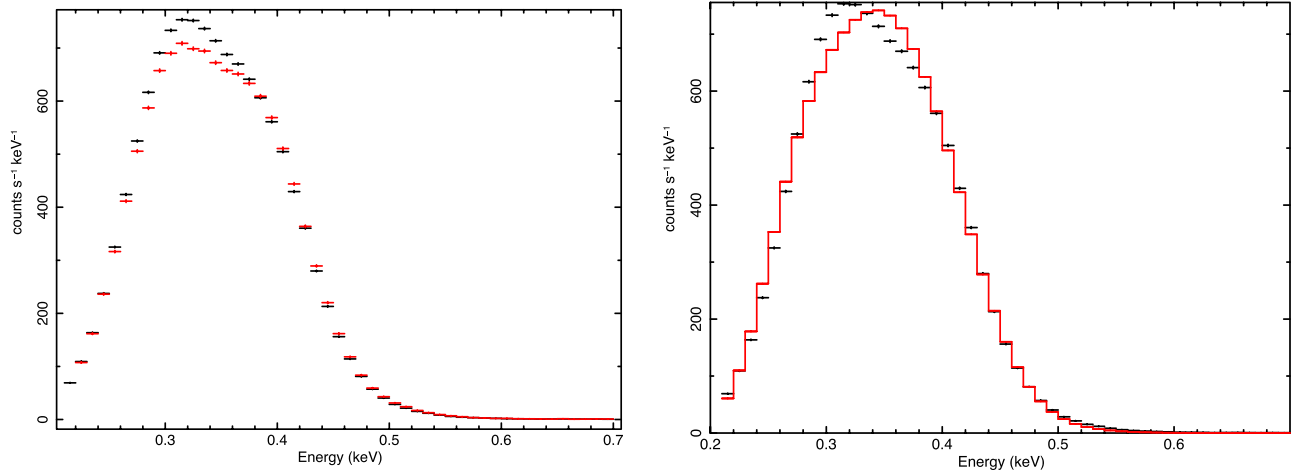
Figure 17. Spectra of YZ Ret observed on 2020 September 28 (in black) and on 2020 September 29 (in red) on the left, and on the right, the 29 September spectrum fitted with an atmospheric model (see text). We did not obtain a rigorous fit, but we could at least conclude that the X-ray flux is orders of magnitude lower than that of a shell-burning WD.

The bolometric luminosity would be only $\simeq 3 \times 10^{35}$ erg s^{-1} at distance of 2.7 kpc.

An observation with XMM-Newton, including use of the RGS grating and done 5 days earlier, explains the low flux: the system must be at high inclination, because no stellar continuum was detected. The spectrum was an emission-line one (Sokolovsky et al. 2021), probably due to photoionized ejecta and with no spectral signatures of shocked material in the collisional ionization equilibrium. Although this conclusion cannot be reached by examining our NICER broadband spectrum, the bolometric luminosity derived is of order 1/1000 of that expected for a burning WD atmosphere, about the same as in the XMM-Newton observation, so clearly this does not support the possibility that the spectrum changed, and the central WD SSS spectrum emerged during the 5 days intercurring between our NICER exposures and the data taken by Sokolovsky et al. (2021). In a different project collaboration, some of us observed the nova after another month with the Chandra LETG, and although the spectrum had considerably changed and softened in comparison with the observations reported by Sokolovsky et al. (2021) and with our NICER broadband spectra, it was, once again, an emission-line one, without a measurable stellar continuum (Drake et al. 2020; and M. Orio et al. 2022c, in preparation).

6. Conclusions

We have observed four SSS with NICER, two persistent sources in close binaries and two transient ones (two novae). The types of objects that we observed span almost all the types of WD binaries. The two close binaries appear to be, respectively, a cataclysmic-variable-like binary with possibly an unusually massive donor, clearly observed at low inclination (CAL 83), and a short-period symbiotic with a yellow donor (MR Vel). The two novae are very likely to being also an IP (V167Her) and a VY Scl nova-like (YZ Ret).

1. The two SSS non-nova close binaries, specifically MR Vel, and CAL 83 in its most common *high* state, had almost unvaried SSS spectra since the last observation performed 21 and 13 yr ago, respectively. MR Vel was observed with almost the same X-ray flux. Although the flux of CAL 83 varies and there are occasional minima

when the SSS becomes undetectable, the maximum flux is also about the same. It is remarkable that this source has not been observed to change significantly over 40 yr of X-ray observations.

2. The large deviations from the continuum of a WD atmosphere and especially the orders of magnitude lower SSS flux of YZ Ret indicates that the WD was never observed in this nova. This is understood if the nova system is observed at high inclination (see Ness et al. 2013). In agreement with the detection of an emission-line spectrum with X-ray gratings close to the time of the NICER observations and even much later, we attribute the SSS flux to the ejecta, which may have been either shocked or photoionized. Given the repeated observations with different satellites at different post-outburst times, we rule out with confidence that a very short-lived SSS phase with WD emission was ever observable for this nova.

3. The $\simeq 67$ s period of CAL 83 is only measurable in X-rays, and it has an irregular drift in length, by about 3%. Our simulations and a rigorous statistical analysis were not conclusive using the short NICER exposures, but by going back to the most recent XMM-Newton exposure, which was much longer and without interruptions, we found that this drift appears to be real and not an artifact of varying amplitude, although the amplitude of the modulations is also often observed to vary.

4. We confirm the evidence pointing to rotation of a magnetic WD as the cause of the modulation of V1674 Her, although in outburst the X-ray luminosity was not due to accretion onto the pole, and only originated in shell-burning. Thus, the WD superficial temperature may not have been homogeneous during the SSS phase, explaining also the difficulty in obtaining a unique and rigorous spectral fit.

5. The flux of V1674 Her had irregular fluctuations superimposed on the regular modulation, confirming the aperiodic variability detected in other nova SSS (e.g., N SMC 2016, Orio et al. 2018; and N LMC 2009 Orio et al. 2021).

6. Because of superimposed emission lines—revealed by a Chandra high-resolution spectrum—we were not able to

obtain a rigorous fit to most of the NICER spectra. Although the SSS spectrum of V1674 Her was "harder" than the SSS spectra of other novae, with the higher S/N and better supersoft response of NICER, we could not confirm the extremely high peak temperature of ≃1,450,000 K suggested by fitting Swift spectra (Drake et al. 2021).

7. Comparing the V1674 Her count rate and spectrum around maximum and minimum of the ≃501 s period, we find that the soft flux is not more absorbed at minimum, so the flux periodic variation is not due to periodically varying absorption. The interpretation that we suggest is that there is a *SSS-obscure* region, which has a much lower effective temperature and does not emit X-rays, possibly around the equator, with a sharp gradient between the SSS and non-SSS regions. The SSS regions must occupy a large portion of the surface, because the SSS flux does not disappear during the minima.

8. The 501 s (≃8.35 minutes) period in V1674 Her was constant (within the precision of our timing analysis) during the post-eruption, luminous SSS phase, and a very close period was measured in the optical in quiescence and in outburst. Within the precision of the NICER data, we could not confirm the putative spin-up of the WD after the outburst.

9. The fading of V1674 Her without significant spectral changes indicates that the SSS emitting region shrunk before cooling, a phenomenon suggested to occur also in other *magnetic novae*.

10. We only observed periodic modulations in two SSS (nova V1674 Her and the non-nova close binary CAL 83) in which there are clear indications that we observed the WD surface, while no such modulations were measured in two sources (again, a nova—YZ Ret—and a non-nova —MR Vel) in which we only observed a wind or an outflow. Considering also that the oscillations were never observed in other SSS whose spectrum is dominated by emission lines, and whose flux is much lower than in SSS in which the WD atmospheric continuum was observed, this pinpoints at the root cause of the periodic flux modulations as a phenomenon occurring on the WD surface or very close to it. Of course, there are also nova and non-nova SSS in which the WD was observed, but periodic modulations were never measured (see Ness et al. 2015, who list 18 SSS in which they searched for ≃ minute long oscillations, finding them only in 5 of them, with a duty cycle even as short as 11%). Only 3 out of the 18 sources in this paper (CAL 87, U Sco, and V959 Mon) are at high inclination, and only CAL 87 has a X-ray spectrum that is completely dominated by emission lines like MR Vel and YZ Ret. However, there are a few caveats. First of all, 5 other of those 18 sources show modulations of the X-ray flux with tens of minutes (see Table 1), bringing the total number of X-ray sources with quasi-periodic or periodic SSS modulations to 10 out of 18. If the modulations with periods of tens of minutes and those with ≃1 minute long oscillations are mutually exclusive, as in this sample of SSS, this may be a clue to a rotational nature of the shorter oscillations, per analogy with the longer ones. A parameter to notice is the effective temperature of the nonperiodic SSS, as estimated in the papers referenced in Table 1. We find

that, on average, they have a lower temperature, although there is an overlap with the range of temperature of the periodic sources. The lower average temperature of the nonperiodic SSS means that also their average X-ray luminosity is lower, hindering the timing analysis because of the lower S/N. Finally, we note that the "duty cycle" (the fraction of time in which the modulation is measurable) of the two sources observed with NICER and described in this paper is about 70% for CAL 83 and 100% for V1674 Her, higher than all measurements of Ness et al. (2015). For the recent outburst of RS Oph, in a separate, still unpublished paper by M. Orio et al. (2022c, in preparation), we found a 100% duty cycle of a ≃35 s oscillations, compared to only ≃16% found in 2006 by Ness et al. (2015) with lower S/N data. We can speculate that the variable amplitude of the period may make the modulation undetectable when the S/N of the measurement is low, the amplitude of the fluctuation is small, and the period is short. Does the modulation really disappear for part of the time, and is it really not present in almost half of the SSS with an observable WD? We would like to argue that the jury is still out, and that NICER with its high S/N may allow for the answer in the next few years, with more observations of SSS.

ORCID iDs

M. Orio ⓘ https://orcid.org/0000-0003-1563-9803
K. Gendreau ⓘ https://orcid.org/0000-0001-7115-2819
G. J. M. Luna ⓘ https://orcid.org/0000-0002-2647-4373
S. Pei ⓘ https://orcid.org/0000-0002-0851-8045
E. Behar ⓘ https://orcid.org/0000-0001-9735-4873
J. Mikolajewska ⓘ https://orcid.org/0000-0003-3457-0020
T. E. Strohmayer ⓘ https://orcid.org/0000-0001-7681-5845

References

Adamczak, J., Werner, K., Rauch, T., et al. 2012, A&A, 546, A1
Aydi, E., Buckley, D. A. H., Chomiuk, L., et al. 2020, ATel, 13867, 1
Aydi, E., Orio, M., Beardmore, A. P., et al. 2018, MNRAS, 480, 572
Bailer-Jones, C. A. L., Rybizki, J., Fouesneau, M., Demleitner, M., & Andrae, R. 2021, yCat, 1352, 0
Bailer-Jones, C. A. L., Rybizki, J., Fouesneau, M., Mantelet, G., & Andrae, R. 2018, AJ, 156, 58
Bearda, H., Hartmann, W., Ebisawa, K., et al. 2002, A&A, 385, 511
Beardmore, A. P., Page, K. L., Markwardt, C. B., et al. 2019, ATel, 13086, 1
Booth, R. A., Mohamed, S., & Podsiadlowski, P. 2016, MNRAS, 457, 822
Chiosi, E., Orio, M., Bernardini, F., Henze, M., & Jamialahmadi, N. 2014, MNRAS, 443, 1821
Córsico, A. H., & Althaus, L. G. 2014, ApJL, 793, L17
Crampton, D., Cowley, A. P., Hutchings, J. B., et al. 1987, ApJ, 321, 745

Dobrotka, A., & Ness, J. U. 2017, MNRAS, 467, 4865
Drake, J. J., Ness, J.-U., Page, K. L., et al. 2021, ApJL, 922, L42
Drake, J. J., Orio, M., Bearmore, A., et al. 2020, ATel, 14214, 1
Drake, J. J., Wagner, R. M., Starrfield, S., et al. 2003, ApJ, 584, 448
Greiner, J., & Di Stefano, R. 2002, A&A, 387, 944
Güver, T., & Özel, F. 2009, MNRAS, 400, 2050
Hessman, F. V. 2000, NewAR, 44, 155
King, A. R., & Cannizzo, J. K. 1998, ApJ, 499, 348
Lanz, T., Telis, G. A., Audard, M., et al. 2005, ApJ, 619, 517
Leibowitz, E., Orio, M., Gonzalez-Riestra, R., et al. 2006, MNRAS, 371, 424
Li, K.-L. 2021, ATel, 14705, 1
Li, K.-L., Kong, A., Aydi, E., et al. 2020, ATel, 13868, 1
Linnell Nemec, A. F., & Nemec, J. M. 1985, AJ, 90, 2317
Livio, M. 1998, in ASP Conf. Ser. 137, Wild Stars in the Old West, ed.
    S. Howell, E. Kuulkers, & C. Woodward (San Francisco, CA: ASP), 264
Livio, M., & Pringle, J. E. 1994, ApJ, 427, 956
Löbling, L., Rauch, T., Miller Bertolami, M. M., et al. 2019, MNRAS,
    489, 1054
Long, K. S., Helfand, D. J., & Grabelsky, D. A. 1981, ApJ, 248, 925
Maccarone, T. J., Beardmore, A., Mukai, K., et al. 2021, ATel, 14776, 1
Mennickent, R. E., Matsumoto, K., & Diaz, M. 2003, A&A, 402, 315
Mereghetti, S., Pintore, F., Rauch, T., et al. 2021, MNRAS, 504, 920
Mereghetti, S., Tiengo, A., Esposito, P., et al. 2009, Sci, 325, 1222
Mikołajewska, J., Iłkiewicz, K., Gałan, C., et al. 2021, MNRAS, 504, 2122
Motch, C. 1998, A&A, 338, L13
Motch, C., Bearda, H., & Neiner, C. 2002, A&A, 393, 913
Mroz, P., Burdge, K., Roestel, J. v., et al. 2021, ATel, 14720, 1
Munari, U., Valisa, P., & Dallaporta, S. 2021, ATel, 14704, 1
Nelson, T., Orio, M., Cassinelli, J. P., et al. 2008, ApJ, 673, 1067
Ness, J. U., Beardmore, A. P., Osborne, J. P., et al. 2015, A&A, 578, A39
Ness, J. U., Osborne, J. P., Dobrotka, A., et al. 2011, ApJ, 733, 70
Ness, J. U., Osborne, J. P., Henze, M., et al. 2013, A&A, 559, A50
Ness, J. U., Starrfield, S., Burwitz, V., et al. 2003, ApJL, 594, L127
Odendaal, A., & Meintjes, P. J. 2017, MNRAS, 467, 2797
Odendaal, A., Meintjes, P. J., Charles, P. A., & Rajoelimanana, A. F. 2014,
    MNRAS, 437, 2948
Orio, M. 2013, AstRv, 8, 71
Orio, M., Dobrotka, A., Pinto, C., et al. 2021, MNRAS, 505, 3113
Orio, M., Nelson, T., Bianchini, A., Di Mille, F., & Harbeck, D. 2010, ApJ,
    717, 739
Orio, M., Ness, J. U., Dobrotka, A., et al. 2018, ApJ, 862, 164
Osborne, J. P., Borozdin, K. N., Trudolyubov, S. P., et al. 2001, A&A,
    378, 800

Osborne, J. P., Page, K. L., Beardmore, A. P., et al. 2011, ApJ, 727, 124
Page, K. L. 2012, MmSAI, 83, 815
Page, K. L., Kuin, N. P. M., Beardmore, A. P., et al. 2020, MNRAS, 499, 4814
Patterson, J., Epstein-Martin, M., Vanmunster, T., & Kemp, J. 2021, ATel,
    14856, 1
Pei, S., Luna, G. J. M., Orio, M., et al. 2021a, ATel, 14798, 1
Pei, S., Orio, M., Gendreau, K., et al. 2020, ATel, 14067, 1
Pei, S., Orio, M., Gendreau, K., et al. 2021b, ATel, 14901, 1
Pei, S., Orio, M., Ness, J.-U., & Ospina, N. 2021c, MNRAS, 507, 2073
Peretz, U., Orio, M., Behar, E., et al. 2016, ApJ, 829, 2
Popham, R., & di Stefano, R. 1996, in Accretion Disks in Supersoft X-Ray
    Sources, ed. J. Greiner, Vol. 472 (Berlin: Springer), 65
Popov, S. B., Mereghetti, S., Blinnikov, S. I., Kuranov, A. G., &
    Yungelson, L. R. 2018, MNRAS, 474, 2750
Prigozhin, G., Gendreau, K., Doty, J. P., et al. 2016, Proc. SPIE, 9905, 99051I
Rajoelimanana, A. F., Charles, P. A., Meintjes, P. J., Odendaal, A., &
    Udalski, A. 2013, MNRAS, 432, 2886
Rauch, T., Orio, M., Gonzales-Riestra, R., et al. 2010, ApJ, 717, 363
Rohrbach, J. G., Ness, J. U., & Starrfield, S. 2009, AJ, 137, 4627
Scargle, J. D. 1982, ApJ, 263, 835
Schmidtke, P. C., & Cowley, A. P. 2001, AJ, 122, 1569
Schmidtke, P. C., Cowley, A. P., Taylor, V. A., Crampton, D., &
    Hutchings, J. B. 2000, AJ, 120, 935
Smith, V. V., Pereira, C. B., & Cunha, K. 2001, ApJL, 556, L55
Sokolovsky, K. V., Li, K.-L., Lopes de Oliveira, R., et al. 2021, arXiv:2108.
    03241
Southwell, K. A., Livio, M., Charles, P. A., O'Donoghue, D., &
    Sutherland, W. J. 1996, ApJ, 470, 1065
Starrfield, S., Timmes, F. X., Iliadis, C., et al. 2012, BaltA, 21, 76
Sun, B., Orio, M., Dobrotka, A., et al. 2020, MNRAS, 499, 3006
Trudolyubov, S. P., & Priedhorsky, W. C. 2008, ApJ, 676, 1218
van den Heuvel, E. P. J., Bhattacharya, D., Nomoto, K., & Rappaport, S. A.
    1992, A&A, 262, 97
Wolf, W. M., Bildsten, L., Brooks, J., & Paxton, B. 2013, ApJ, 777, 136
Wolf, W. M., Townsend, R. H. D., & Bildsten, L. 2018, ApJ, 855, 127
Worters, H. L., Eyres, S. P. S., Bromage, G. E., & Osborne, J. P. 2007,
    MNRAS, 379, 1557
Wu, K., Wickramasinghe, D. T., & Warner, B. 1995, PASA, 12, 60
Yaron, O., Prialnik, D., Shara, M. M., & Kovetz, A. 2005, ApJ, 623, 398
Zemko, P., Ciroi, S., Orio, M., et al. 2018, MNRAS, 480, 4489
Zemko, P., Mukai, K., & Orio, M. 2015, ApJ, 807, 61
Zemko, P., Orio, M., Mukai, K., et al. 2016, MNRAS, 460, 2744
Zemko, P., Orio, M., Mukai, K., & Shugarov, S. 2014, MNRAS, 445, 869